Bioactive Materials 21 (2023) 340–357

Contents lists available at ScienceDirect

Bioactive Materials

journal homepage: www.keaipublishing.com/en/journals/bioactive-materials

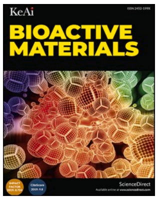

Reciprocal interaction between vascular niche and sweat gland promotes sweat gland regeneration

Xingyu Yuan [a,b,c,1], Xianlan Duan [a,b,c,1], Enhejirigala [d,e,1], Zhao Li [b,c,1], Bin Yao [b,c,f], Wei Song [b,c], Yuzhen Wang [b,c,g], Yi Kong [b,c], Shijun Zhu [a,b], Fanliang Zhang [b,c], Liting Liang [b], Mengde Zhang [b,c], Chao Zhang [a,b], Deling Kong [h], Meifeng Zhu [h], Sha Huang [b,*], Xiaobing Fu [a,b,c,i,**]

[a] *School of Medicine, Nankai University, 94 Weijin Road, Tianjin, 300071, PR China*
[b] *Research Center for Tissue Repair and Regeneration Affiliated to the Medical Innovation Research Department, PLA General Hospital, 28 Fuxing Road, Beijing, 100853, PR China*
[c] *PLA Key Laboratory of Tissue Repair and Regenerative Medicine and Beijing Key Research Laboratory of Skin Injury, Repair and Regeneration, Chinese PLA General Hospital and PLA Medical College, 51 Fucheng Road, Beijing, 100048, PR China*
[d] *College of Graduate, Tianjin Medical University, Tianjin, 300070, PR China*
[e] *Institute of Basic Medical Research, Inner Mongolia Medical University, Hohhot, 010110, Inner Mongolia, PR China*
[f] *Academy of Medical Engineering and Translational Medicine, Tianjin University, 92 Weijin Road, Tianjin, 300072, PR China*
[g] *Department of Burn and Plastic Surgery, Air Force Hospital of Chinese PLA Central Theater Command, Datong, 037000, Shanxi, PR China*
[h] *College of Life Science, State Key Laboratory of Medicinal Chemical Biology, Key Laboratory of Bioactive Materials of Ministry of Education, Nankai University, 94 Weijin Road, Tianjin, 300071, PR China*
[i] *Research Unit of Trauma Care, Tissue Repair and Regeneration, Chinese Academy of Medical Sciences, 2019RU051, Beijing, 100048, PR China*

ARTICLE INFO

Keywords:
Vascular niche
3D bioprinting
Sweat gland-vasculature interaction model
ECM scaffold
Sweat gland regeneration

ABSTRACT

The incorporation of vasculature is known to be effective in tissue or organ functional regeneration. However, a vague understanding of the interaction between epidermal appendages and their vascular niches is a foremost obstacle to obtaining sweat gland (SG)-specific vasculature units. Here, we map their precise anatomical connections and report that the interplay between SG cells (SGCs) and the surrounding vascular niche is key for glandular development and homeostasis maintenance. To replicate this interplay *in vitro*, we used three-dimensional (3D) bioprinting to generate reproducible SGC spheroids from differentiated adipose-derived mesenchymal stem cells (ADSCs). With dermal microvascular endothelial cells (DMECs), sacrificial templates made from poly (ε-caprolactone) (PCL) were fabricated to pattern the vascular niche. This interplay model promoted physiologically relevant vascularized glandular morphogenesis *in vitro* and *in vivo*. We identified a reciprocal regulatory mechanism for promoting SGs regeneration via contact-independent cell communication and direct cell-cell interactions between SGs and the vasculature. We envision the successful use of our approach for vascularized organ regeneration in the near future.

1. Introduction

In recent years, it is increasingly recognized that blood vessels, especially the capillary beds of tissues or organs, are not just passive and permissive conduits for delivering blood [1,2]. These tissue- or organ-specific vasculatures establish specialized vascular niches which release sets of endothelium-derived growth factors and angiocrine factors (i.e., cytokines, chemokines, extracellular matrix components,

---

Peer review under responsibility of KeAi Communications Co., Ltd.

* Corresponding author. Research Center for Tissue Repair and Regeneration Affiliated to the Medical Innovation Research Department, PLA General Hospital, 28 Fuxing Road, Beijing, 100853, PR China.

** Corresponding author. Research Center for Tissue Repair and Regeneration Affiliated to the Medical Innovation Research Department, PLA General Hospital, 28 Fuxing Road, Beijing, 100853, PR China.

E-mail addresses: stellarahuang@sina.com (S. Huang), fuxiaobing@vip.sina.com (X. Fu).

[1] These authors contributed equally to this work.

https://doi.org/10.1016/j.bioactmat.2022.08.021
Received 5 June 2022; Received in revised form 20 August 2022; Accepted 25 August 2022

exosomes, etc.) [1]. And all these cues provide signals for the induction, specification, patterning and guidance of tissue or organ regeneration [1,3–7]. Although the angiocrine functions of tissue- or organ-specific vasculatures have been well defined in many fields of regenerative medicine (e.g., lungs, liver, bones, adipose tissues and endocrine glands), the contribution of vascular niches to the modulation of homeostasis and regeneration in epithelial appendages (e.g., sweat glands (SGs)) are still unsettled [1,4,5].

SGs are skin appendages with extremely poor regenerative potential and are often challenging to regenerate due to congenital diseases, genetic mutations, and severe burns or trauma [8–10]. In clinical studies, especially for hypertrophic scars, the rate of scar repairing far exceeds SG regeneration and forms a barrier that hinders the latter's renewal, ultimately severely reducing the patient's quality of life [11]. SGs play a vital role in thermoregulation through sweating when we exercise or survive in an extreme climate, which requires an abundant blood supply [12–14]. In exocrine glands, the unique anatomical distribution of glands and microvasculature is the premise for the rapid secretion of substances. The exploration of the anatomy and relationship between SGs and blood vessels began with histological studies in the 1950s [15]. When researchers performed frozen section, silver impregnation and corrosion casting to demonstrate the microvasculature around the SGs, they observed the proximity of capillaries and SGs, and inferred that the former just play a role in the supply and reabsorption of sweat [13,15–17]. Since then, a few follow-up reports revealing some ambiguous relationship between SGs and their specific vasculature in the last decade [18–21]. However, our current vague understanding of the relationship between SGs and their adjacent tissues, especially the microvascular network, largely limits thinking about SG regeneration strategies.

Tissue clearing technique, a valuable tool for whole-body imaging, enables visualization of opaque organs or tissues in three dimensions by regulating their transparency, which has been commonly applied to mine detailed anatomical information about complex tissues or organs (e.g., bones, teeth, brain, and skin) [22–24]. CellPhoneDB, a manually curated repository of ligands, receptors, and their interactions integrated with a statistical framework to infer biologically relevant interacting pairs from single-cell transcriptomic data, that was developed to investigate how the context-dependent crosstalk of different cell types enables physiological processes to proceed [25–27]. With this perspective, both the tissue clearing technique and CellPhoneDB are ideal tools for the purpose which enable to study the detailed anatomical relationship and complex signal networks between SGs and their vasculature. In addition, some emerging engineering techniques in recent years also provide the possibility to simulate the interaction between SGs and vasculature *in vitro* and reconstruct SGs *in vivo*. For example, microfluidic chips enabled to dynamically observe the biological behavior of two interacting cells in situ. Constructing vascular networks using engineered templates is a flexible and controllable strategy to mimic natural vascular features and trigger the functional regeneration of corresponding tissues or organs [4,28–30]. Furthermore, three-dimensional (3D) bioprinting is an evolutionary additive manufacturing technique that enables fabrication of biomimetic, multiscale, multi-cellular tissues with heterogeneous cells and highly complex tissue microenvironment [31]. It is a powerful tool for tissue engineering and can significantly improve the efficiency of stem cell differentiation into SGs, providing a sufficient and stable cell source for the study of SG-vascular interactions [32–35].

In this study, we initially determined the anatomy of SGs and their surrounding microvasculature using tissue clearing technique, and clarified the molecular interactions between glandular and endothelial cells in their resident microenvironment with CellPhoneDB. Then, we employed the 3D bioprinted extracellular matrix (ECM) mimics to facilitate the specific SG differentiation of adipose-derived mesenchymal stem cells (ADSCs) and applied Transwell devices and 3D microfluidic chips to elucidate the effect of this interaction on the formation and function of SGs and their specific vascular network. Finally, we generated an angiogenic ECM scaffold with a polymer-based sacrificial template and mimicked the SG-vascular physiological interactions *in vitro* and promoted physiologically relevant vascularized glandular morphogenesis *in vivo*. We hypothesize that the direct interaction of SGs and their specific vasculature may serve as valuable analogs to clarify the interplay and recapitulate a complete and physiological SG regenerative microenvironment.

2. Materials and methods

2.1. Study design

This study's primary objective and design were first to investigate whether there is an interaction between SGs and their surrounding microvasculature. Then, to further determine the impact of this interplay on the formation and function of SGs and their specific vascular networks. Finally, to explore this interaction's effects on promoting SG regeneration. The main aims were as follows: (i) resolving the anatomy and interactions of SGs and their surrounding microvasculature; (ii) clarifying SG-vascular indirect and direct interactions; (iii) mimicking the SG-vascular physiological interactions *in vitro*; (v) promoting physiologically relevant vascularized glandular morphogenesis *in vivo*.

2.2. Human subjects

One male and two female patients clinically diagnosed with hypertrophic scars were enrolled in this study. Their ages ranged from 20 to 33, with a median age of 25. All normal human skin tissues were obtained from a 5 × 5-mm^2 skin biopsies with the informed consent of the patients, and the studies were approved by the Ethics Committee of the Chinese PLA General Hospital (Beijing, China; project No. ChiCTR2000033157). The clinical characteristics of these donors and the number of cells used for single-cell sequencing analysis were summarized in Table S1.

2.3. Animals

Adult mice (6-8-weeks-age) with genotypes including C57BL/6, *CAG-tdTomato* were purchased from GemPharmatech Biotechnology Co., Ltd, China. Sprague Dawley rats (8-10-weeks-age) were purchased from SPF Biotechnology Co., Ltd. Animals were maintained in a specific-pathogen-free facility of Chinese PLA General Hospital in accordance with the Guide for the Care and Use of Laboratory Animals. All animal experiments were approved by the Institutional Animal Care and Use Committee of Chinese PLA General Hospital (approval number SCXK (BJ)2017–0001).

2.4. Light-sheet imaging

The anatomy of SGs and their surrounding microvasculature was visualized based on the PEGASOS methods [24]. Briefly, adult *CAG-tdTomato* mice were anesthetized with pentobarbital (50 mg kg^{-1}) by an intraperitoneal injection. Hind feet, provided with major interdigital pads, were isolated from the mice after tail vein injection of Lycopersicon Esculentum lectin (500 μg mL^{-1}; Thermofisher, L32472) and transcardiac perfusion. Following tissue fixation with 4% paraformaldehyde (Solarbio, China) and phosphate buffered saline (PBS) rinse for 24 h, the samples were cleared over 7 days and imaged within the light sheet chamber. All specimens were scanned using a Zeiss Z.1 Light-sheet microscope equipped with W Plan-Apochromat 20 × /1.0 objective at a 2 μm step size. Image collection, processing and 3D rendering was carried out with a Precision T7600 workstation (Dell, USA). 3D reconstruction images and movies were generated using Imaris 9.7 (Bitplane, Switzerland). Stack images were generated using the "volume rendering" function. 3D images were generated using the "snapshot" function. Movies were generated using "animation" function.

2.5. CellPhoneDB analysis

The CellPhoneDB method described in the previous report was carried out to predict cross-talk between SG and their adjacent microvasculature based on the single-cell transcriptomics data of normal human skin tissues [36,37]. First, the cell type labels of all cells were randomly permuted and the mean of the average receptor expression and the average ligand expression for each pair of cell types was calculated. A P value for the likelihood that a given interaction is specific for a certain cell type pair can then be obtained by taking the proportion of means from a null distribution of calculation that are greater than or equal to the observed mean. Significant interactions can then be prioritized on the basis of their P value. Biologically relevant interactions can then be chosen on the basis of their average expression level.

2.6. Gene ontology (GO) analysis

To further elucidate the biological functions of SG-vasculature communication, GO enrichment analyses were performed using Metascape (https://metascape.org) with the following customizations: a background gene list of ligand-receptor was provided, and the GO Biological Processes database was used for testing gene enrichment. Metascape performs hierarchical clustering of the enriched terms, showing the most significant term within a cluster as the representative term in the enrichment results.

2.7. Bioprinting and SG lineage differentiation

Bioprinting and SG induction were performed following the similar procedures in previous report. Briefly, the bioink was first prepared with sodium alginate (Sigma-Aldrich; 1%, w/v in PBS) and gelatin (Sigma-Aldrich; 3%, w/v in PBS) following our previous optimization studies [38,39]. Then a mixture of single-cell suspension of ADSCs (1×10^7 cells mL^{-1}) and plantar dermis (PD) ECM solution (58 μg mL^{-1}) was gently mixed with the bioink, and gel for 1 h at 4 °C. Next, the cell-containing bioink was continuously bioprinted into cylindrical constructs in six-well polystyrene plates (Corning, USA) by using an extrusion-based 3D bioprinter (Regenovo, China). All cylindrical constructs were 20 mm in diameter and four layers in height and bioprinted following the previously optimized process parameter [32]. Following the 3D bioprinting procedure, bioprinted constructs were immersed in the calcium chloride (2.5%, w/v) to crosslink for 3 min, then washed three times in Dulbecco's modified Eagle medium (DMEM; Gibco, USA). Finally, the crosslinked cell-containing constructs were cultured with SG induction medium (SGIM; Table S2) at 37 °C in a 5% CO_2 standard incubator and the medium was exchanged every other day. Cell morphology was observed and recorded using a phase-contrast microscope (Leica DMI4000B, Germany).

2.8. Gene expression analysis

To harvest the cells in bioprinting constructs, a mixture of sodium citrate (55 mM), ethylenediaminetetraacetic acid disodium salt (20 mM) and sodium chloride (150 mM) was used to dissolve the 3D constructs for 5 min. After gently shaking and centrifugation, the supernatant was removed and precipitates were collected for further analysis. Total RNA was extracted from the harvested cells by using TRIzol reagent (Invitrogen, USA). Reverse transcription was carried out using PrimeScript RT reagent Kit with gDNA Eraser (Takara, China). Quantitative analysis of gene expression was performed using TB Green Premix Ex Taq II (Takara, China) on a QuantStudio 5 system (Applied Biosystems, USA). The expression level of target genes was normalized to *Gapdh* and calculated with the $2^{-\Delta\Delta CT}$ method. All the designed primers for target genes were list in Table S3. At least three replicates were conducted to analyze significance.

2.9. ECM scaffold fabrication

ECM scaffolds were fabricated as described previously [40]. For angiogenic ECM scaffolds (AES) preparation, the intersectional poly (ε-caprolactone) (PCL; Sigma-Aldrich, Mn = 70,000–90,000 Da) microfiber templates were first fabricated using a homemade melt-spinning apparatus. PCL pellets were added into the charging barrel equipped with a 15 G needle, heated to 100 °C and melted until transparency. Driven by a syringe pump, the PCL fibers were extruded out at a flow rate of 6 mL h^{-1} and collected onto a rotating rod (8.0 cm in diameter) for 30 min. Then the templates were implanted subcutaneously in rats for 4 weeks to allowed cellularization and ECM deposition. Subsequently, the implant constructs (Fiber-Cell-ECM) were harvested, dehydrated sequentially in 40%, 60%, 80%, and 100% ethanol series, and immersed in chloroform to remove polymers. Following 48 h of elution, the porous constructs (Cell-ECM) were obtained and then rehydrated with 100%, 80%, 60%, and 40% until sterile water. After that, the constructs were sequentially treated with 1% sodium dodecyl sulfate (SDS; Solarbio, China) solution and mixture of 1% deoxyribonuclease I (Sigma-Aldrich) and ribonuclease (Sigma-Aldrich) solution for 12 h at 37 °C to achieve decellularization. Finally, the ECM scaffolds with interconnected network of microchannels were obtained after rinsed with PBS and freeze drying using a freeze dryer (Terroni, Brazil). For nonangiogenic ECM scaffolds (NES) preparation, the PCL templates were first fabricated using a homemade electrospinning apparatus with the following conditions: 30% (w/v) PCL solution in methanol-chloroform solution (5:1, v/v), 21G needle, a voltage of 16 kV, a collection distance of 18 cm, electrospinning time of 15 min. Then the templates were treated with the similar methods to generate the decellularized scaffolds. All the freeze-dried scaffolds were stored at −20 °C until further use.

2.10. Cell infiltration assay

Cell infiltration assay were performed according to the similar procedures in previous report [41]. After 7 days of culture, DMEC containing-scaffolds were fixed in 4% paraformaldehyde for 20 min, washed three times with PBS, and stained with CD31 (ab28364, Abcam, 1:100) at 4 °C overnight for microscopy. The infiltration of DMECs was visualized by using a TCS SP8 confocal microscope (Leica, Germany) with a 10 × objective. Three z-stacks were randomly taken in each group at 1 × zoom. The most superficial and the deepest CD31 signals were set as the vertical boundaries of the z-stacks, which were taken at 3 μm intervals. The obtained z-stack images were imported into Imaris 9.7 software. The "spots" function was applied to assign a spot for CD31 fluorescent signal of a single DMEC, enabling the localization of cells in 3D space. A reference frame of XY plane was set at the top of the DMEC monolayer to determine the number and depth of infiltrating spots using Imaris statistical analysis tool.

2.11. Establishment of SG-vasculature interaction model (SVIM)

After being harvested from the 3D constructs using the method described above, 20 μL droplets of induced sweat gland cell (iSGC) suspension (1×10^5 cells mL^{-1}) were seeded on a lid of Petri dish, which was gently inverted and placed on top of the dish containing PBS to maintain a humid atmosphere. Individual cells were aggregated within hours of incubation due to gravity, forming a 3D spheroid. Following 3 days of induction, the collected iSGC spheroids (100 pcs cm^{-2}) were gently seeded on the surface of ECM scaffolds prevascularized with dermal microvascular endothelial cells (DMECs; 1×10^5 cells cm^{-2}) and cultured for another 7 days. The mixed medium of SGIM and endothelial cell growth medium-2 (EGM-2) was exchanged every other day. The

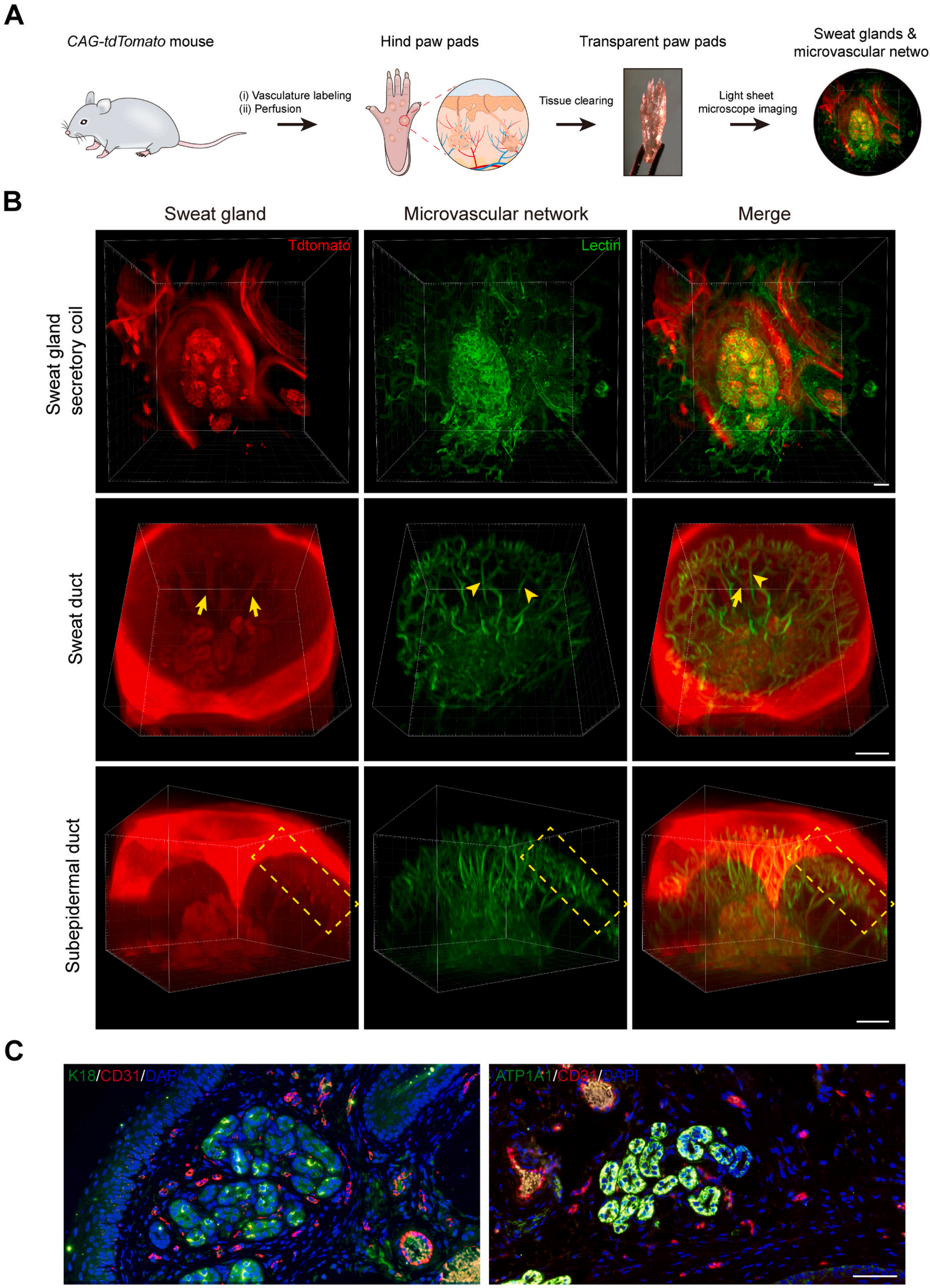

Fig. 1. Determine the anatomy of SGs and their surrounding microvasculature using tissue clearing technique and histological staining. (**A**) Schematic showing 3D imaging of the SG-vasculature anatomical structure by using the tissue-clearing technique. (**B**) Light-sheet microscopy images showing the close proximity of SGs and their vascular beds after optical clearing. Arrows and arrowheads indicate SGs and microvessels, respectively. Dashed boxes highlight the subepidermal ducts and nearby vascular arcades. (**C**) Conventional histological sections confirming the capillaries (CD31) closely surround the SGs (K18 and ATP1A1). CD31, red; K18, ATP1A1, green; DAPI, blue. Scale bars: **B**, 100 μm; **C**, 50 μm.

infiltration depth of iSGC spheroids were quantified with similar method in the cell infiltration assay. 3D reconstruction of SVIM were performed using Imaris software based on CD31 and Keratin 18 (K18; ab668, Abcam, 1:300) fluorescent signal in confocal z-stacks. Likewise, the obtained z-stack images were first imported into Imaris 9.7 software. Then the "spots" function was applied to assign a spot for the CD31 fluorescent signal of a single DMEC to simulate a DMEC. After that, the "surface" function was used to set a rough surface to the K18 fluorescence signal of the iSGC spheroid to simulate the iSGC spheroid. Finally, the spatial positions of points and surface were used to determine whether the DMECs and iSGC spheroids were aggregated. At least three biological replicates were carried in this experiment.

2.12. Transplantation of vascularized spheroids

Green fluorescent protein (GFP)-labeled ADSCs in bioprinting constructs with PD were cultured for 3 days and harvested to form 3D spheroids. Following 3 days of culture, the collected iSGC spheroids were cocultured with DMECs in ECM scaffolds for another 7 days. The vascularized spheroids were manually harvested with a 200 μL pipettor by utilizing a phase-contrast microscope to optimize visualization. The obtained 50 μL spheroids suspension (3000 pcs mL^{-1}) were then injected into the hind paw pads of mice by using Microliter syringes (Hamilton, USA). After 14 days of rearing, the treated paws were excised and carried for further histologic analysis. In addition, in the thermal-injured mouse model, the method was the same except that Tdtomato-labeled DMECs were used.

2.13. Sweat test

The hind paw pads of anesthetized mice were first applied with 2% (w/v) iodine/ethanol solution, then painted with starch/castor oil solution (0.5 g mL^{-1}) after drying. Subsequently, 50 μL of 100 μM acetylcholine (Sigma-Aldrich, USA) was subcutaneously injected into the hind feet to stimulate sweating. Dark sweating spots appeared in 15 min and were recorded immediately.

2.14. Transwell assays

Transwell assays were carried to assess the effects of iSGCs on DMEC migration and infiltration. For infiltration assay, the 3D-printed constructs loading 2×10^5 ADSCs were first placed in lower compartments of 6.5-mm Transwell containing 8.0 μm pore inserts (Corning, USA) and cultured for 3 days. Then, the inserts were pre-coated with Matrigel (Corning, USA) and solidified in 37 °C incubator for 30 min. DMECs were starved for 24 h, resuspended with serum-free medium (SGIM: EGM-2 = 1:1), and seeded into upper compartments at a density of 2×10^5 per well. After coculture for another 36 h, the DMECs were fixed with 4% paraformaldehyde, cells that did not infiltrate were completely removed with a cotton swab. Infiltrated DMECs were stained with 0.1% crystal violet (Solarbio, China) for 30 min and rinsed three times with PBS. For migration assay, the Matrigel coating procedure was skipped, and the cocultivation time was reduced to 20 h. Serum-containing medium and basal medium in tissue culture plate (TCP) were set as positive and negative control in all experiments, respectively. At least 15 randomly selected fields in three replicates were counted to quantify the number of migrated or infiltrated DMECs.

2.15. Microfluidic assays

ADSCs were first digested, counted and resuspended at a concentration of 5×10^6 cells mL^{-1}. 10 μL ADSC suspension was then introduced into one of the medium reservoirs of iSGC-loaded channel (iSGC-C), and sucked into the channel by applying gentle vacuum in the opposite reservoir (t = −3 d). Subsequently, the microfluidic device was tilted 90° and incubated at 37 °C for 30 min to allow ADSCs adhere to Matrigel surface. 200 μL SGIM (with or without PD ECM) was then immediately added to the medium reservoirs of iSGC-C. Upon 3 days of culture, DMECs were also suspended at a density of 5×10^6 cells mL^{-1} and supplemented into the DMEC-loaded channel (DMEC-C) with similar method (t = 0 d). After cell seeding, the microfluidic chip was incubated at 37 °C and 5% CO_2 and continuously monitored for 2 days. During the 5 d assays, the medium was initially replaced daily with SGIM (t = −3 to 0 d) and then with the mixture of SGIM and EGM-2 (t = 1–2 d). Cell morphology was recorded using a phase-contrast microscope at the scheduled time.

2.16. Immunostaining

For fluorescent imaging, the cells, microfluidic chips and tissue samples were first rinsed twice with PBS, fixed in 4% paraformaldehyde for 15 min and permeabilized using 0.3% Triton X-100 for 10 min. To reduce nonspecific background, all samples were then treated with 5% goat serum (Solarbio, China) for 1 h. After that, the cells and tissue samples were incubated with primary antibodies at 4 °C overnight and secondary antibodies at room temperature for 2 h. The microfluidic chips were incubated with primary antibodies and secondary antibodies both at 4 °C for 24 h. The primary antibodies used in these experiments were anti-Keratin 8 (K8, ab32579, Abcam, 1:300), anti-Keratin 14 (K14, ab7800, Abcam, 1:300), anti-K18 (1:300), anti-Keratin 19 (K19, ab52625, Abcam, 1:300), anti-ATPase Na^+/K^+ transporting subunit alpha 1 (ATP1A1, ab7671, Abcam, 1:300), anti-CD31 (1:100) and anti-vascular endothelial (VE)-cadherin (sc-9989, Santa Cruz, 1:100). The secondary antibodies used in these experiments were CoraLite488 conjugated Goat Anti-Mouse IgG (SA00013-1, Proteintech, USA, 1:200), CoraLite488 conjugated Goat Anti-Rabbit IgG (SA00013-2, Proteintech, USA, 1:200), CoraLite594 conjugated Goat Anti-Mouse IgG (SA00013-3, Proteintech, USA, 1:200) and CoraLite594 conjugated Goat Anti-Rabbit IgG (SA00013-4, Proteintech, USA, 1:200). Cell nuclei and F-actin were labeled with 4′,6-diamidino-2-phenylindole (DAPI; Sigma-Aldrich, USA) for 15 min and phalloidin (ab176753, Abcam, 1:1000) for 1 h, respectively. Fluorescent images were captured with a TCS SP8 confocal microscope.

2.17. Statistical analysis

All experiments were performed at least three replicates to determine significance, except the single-cell sequencing was performed in one experiment. Sample sizes are indicated in the figure captions. All data were presented as means ± standard deviation (s.d.). Statistical analyses were performed using GraphPad Prism 7.0 (GraphPad, USA). The two-group comparison was performed by two-tailed *t*-test. The multiple-group comparison was implemented by one- or two-way analysis of variance (ANOVA) with post hoc Tukey test. $P < 0.05$ was considered as a statistically significant, and the significance level was noted as $^*P < 0.05$, $^{**}P < 0.01$, $^{***}P < 0.001$, $^{****}P < 0.0001$.

3. Results

3.1. Anatomical relationship between SGs and the vasculature

To explore how SGs are related to the surrounding vasculature, we first designed the strategy in Fig. 1A to map their precise anatomical relationships. 3D reconstruction of light-sheet microscopy images revealed particularly elaborate capillary networks tightly arranged around the SGs (Fig. 1B and Fig. S1). In detail, cage-shaped microvascular networks were interwoven among the secretory coils of SGs, where blood vessels following the different loops of the coiled tubules and sprouting branches and shunts connecting the other vessels around adjacent loops were observed (Fig. 1B, Fig. S1B, SG secretory coil and Movie S1). Sweat ducts were accompanied from secretory coils toward paw pad surface by one or more microvessels in a parallel arrangement

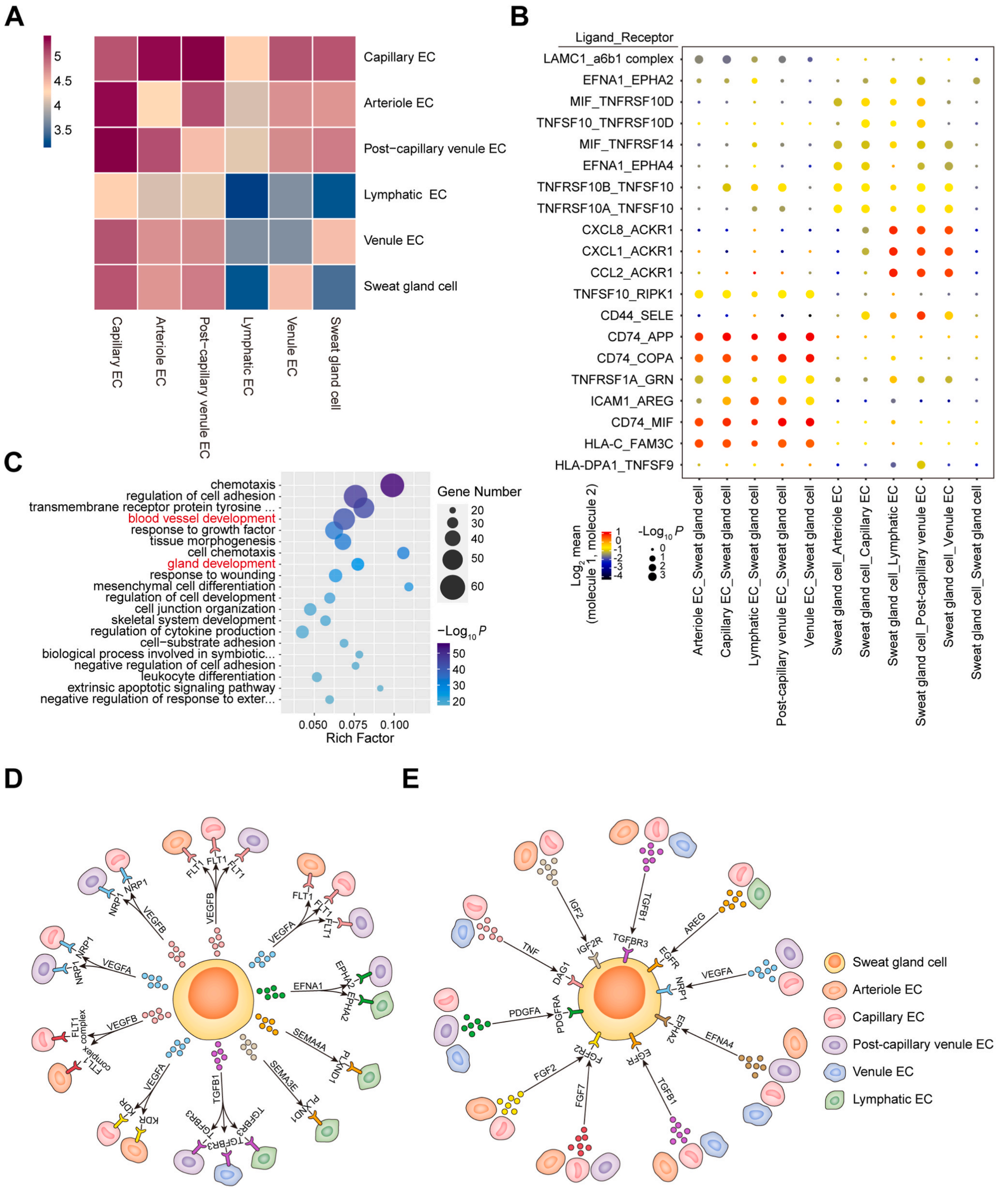

Fig. 2. Analysis of the signaling networks of SG-vasculature communication using CellPhoneDB and GO. (**A**) Heatmap depicting all possible interactions between SGCs and ECs obtained with CellPhoneDB. (**B**) Dot plot showing the top 20 ligand-receptor pairs between SGCs and ECs. Dot size represents the *P* value. Dot color represents the mean of the average expression level of the two interacting molecules in their respective clusters. (**C**) Scatter plot displaying the upregulated receptor and ligand genes by GO enrichment analysis (top 20 GO terms). The rich factor indicates the ratio of the number of genes with significant differences annotated as a specific GO term to all genes annotated as the same GO term. Dot size represents the number of genes with a significant difference enriched in a specific GO term. Dot color represents the *P* value obtained by GO analysis. $P < 0.05$ was used to indicate significant enrichment. (**D**) Diagram summarizing the main signals of SGCs in promoting vascular development. (**E**) Diagram summarizing the main signals of ECs in promoting glandular development.

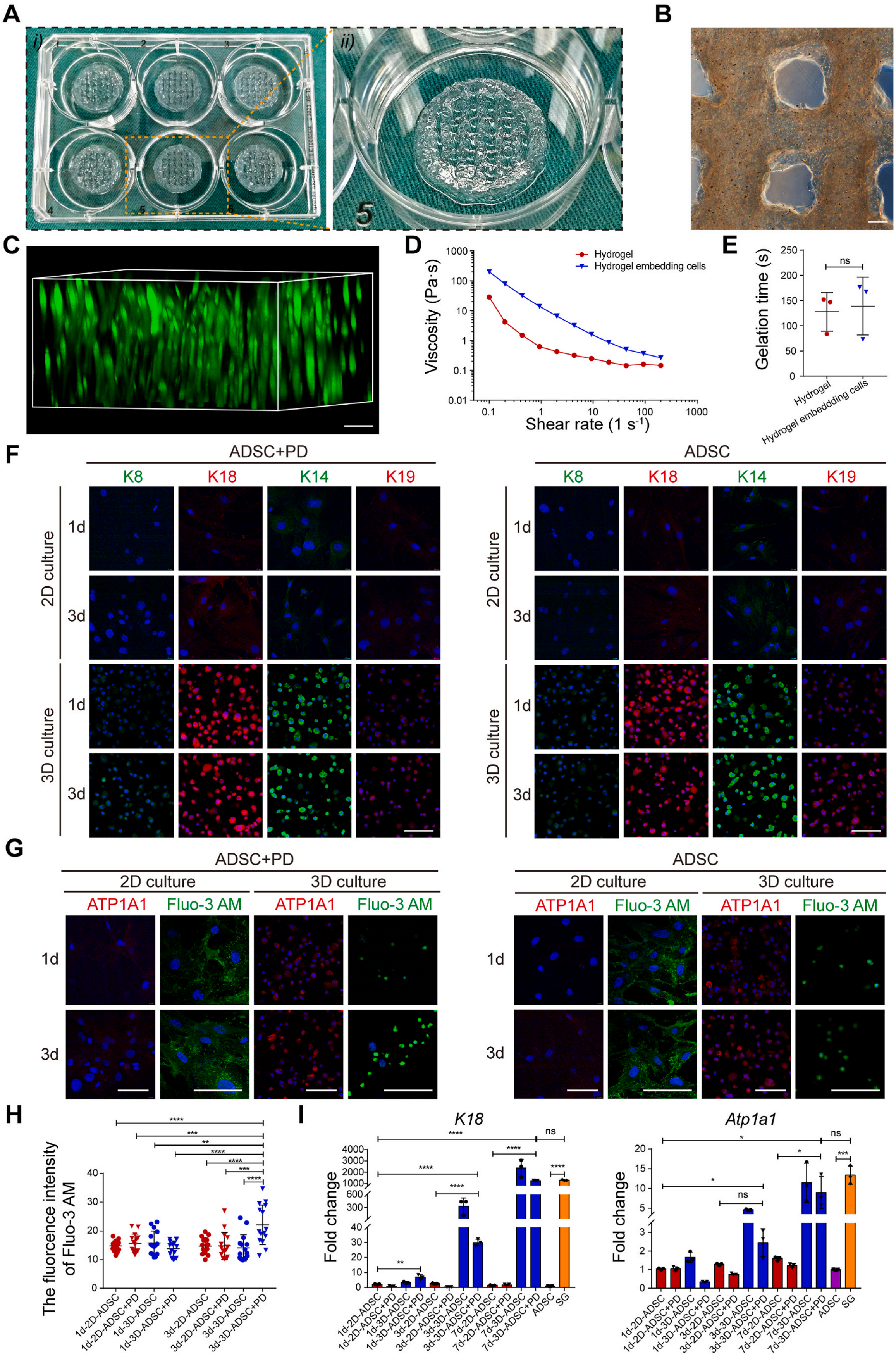

(caption on next page)

Fig. 3. 3D-bioprinted specific ECM microenvironments direct SG differentiation. (A) Overview of the 3D-bioprinted ADSC-loaded constructs. (**B**) Representative microscopic image of the 3D-bioprinted lattices. (**C**) Calcein-AM staining displaying the spatial distribution of ADSCs in the bioprinting constructs. (**D**, **E**) The rheological property and gelation time (n = 3) of bioink before and after embedding cells. (**F**) Comparison of SG-specific markers (including K8, K14, K18, and K19) in cells cocultured with different biochemical (with or without PD) and structural (2D or 3D) cues. K8 and K14, green; K18 and K19, red; DAPI, blue. (**G**) Comparison of SG functional markers (osmoregulation and ion transport) in cells cocultured with different inducing cues. ATP1A1, red; Fluo-3 AM, Ca^{2+} indicator, green; DAPI, blue. (**H**) Dot plot of the geometric mean fluorescence intensity of Fluo-3 AM in cells cocultured with different inducing cues at day 3 (n = 15). (**I**) Transcriptional expression of *K18* and *Atp1a1* in cells that had been treated with different inducing cues at day 1, 3 and 7 (n = 3). The results are presented as mean ± s.d., $^{*}P < 0.05$, $^{**}P < 0.01$, $^{***}P < 0.001$, $^{****}P < 0.0001$. ns, not significant. The two-group comparison was performed by unpaired two-tailed *t*-test. The multiple-group comparison was implemented by two-way ANOVA with Tukey's multiple comparisons test. Scale bars: **B**, 200 μm; **C**, **F**, **G**, 100 μm.

(Fig. 1B, Fig. S1B, Sweat duct and Movie S2). These vessels were connected by cross-shunts and branched at the level of the subpapillary plexus. Furthermore, the straight ducts near the surface of the paw pads were also wrapped by the capillary branches from the vascular arcades under the epidermis (Fig. 1B, Fig. S1B, Subepidermal duct and Movie S3). In general, the adjacent microvascular networks of SGs formed a radial pattern. They seemed to closely follow the contours of SGs tubules, in line with our immunofluorescent staining results labeling endothelial (CD31) and SG (K18 and ATP1A1) markers (Fig. 1C). This unique 3D anatomy may facilitate rapid blood supply to the entire glandular structure of the SGs, thereby accelerating the process of sweat transport and reabsorption [13,15,17].

Supplementary data related to this article can be found at https://doi.org/10.1016/j.bioactmat.2022.08.021.

3.2. Signaling communication between SGs and the vasculature

Given the elaborate SG-vasculature anatomy observed in the paw pads, we further investigated their crosstalk through direct interactions or secreted molecules. To systematically study the interplay between glandular and endothelial cells (ECs) in their resident microenvironment, we predicted the cell-cell communication networks based on CellPhoneDB [25–27]. CellPhoneDB analysis revealed numerous connections between sweat gland cells (SGCs) and ECs (Fig. 2A). This interaction landscape was dominated by the communication of SGCs with vascular ECs rather than lymphatic ECs (Fig. 2A and B and Table S4). To further elucidate the biological functions of SG-vasculature communication, GO analysis of ligand-receptor genes was performed based on the enriched CellPhoneDB results (Fig. 2C and Table S5). These upregulated genes were mainly involved in chemotaxis, cell adhesion, blood vessel development, gland development, wound healing and cell differentiation (Fig. 2C). Focusing on the regenerative applications of SG-vasculature interaction, we identified signals related to the development of blood vessels and glands in the communication network (Fig. 2D and E). In interactive plots, broadly speaking, "proangiogenic" signals, including vascular endothelial growth factor (VEGF), vascular endothelial growth factor receptor (VEGFR), transforming growth factor beta (TGFB), and transforming growth factor beta receptor (TGFBR), were involved in the biological process by which SGs promote blood vessel development via the paracrine system (Fig. 2D and Table S6). Interestingly, the CellPhoneDB analysis also uncovered similar feedback regulation from ECs to SGCs, namely, the angiocrine functions of the microvasculature to promote gland development (Fig. 2E and Table S7), e.g., VEGF, VEGFR, TGFB, TGFBR, insulin like growth factor (IGF), insulin like growth factor receptor (IGFR), fibroblast growth factor (FGF), and fibroblast growth factor receptor (FGFR). Overall, the communication between vascular and glandular cells was complicated and frequent, and the reciprocity between the two is a cornerstone for maintaining glandular homeostasis and repair in time.

3.3. Direct SG differentiation of ADSCs with biochemical and structural synergy effect

Given the difficulty of primary SGC isolation and subculture, to clarify the interplay between SGs and their specific vasculature, we adopted the 3D bioprinting technique with PD ECM to guide the specific SG differentiation of ADSCs (Figs. S2A and B) [42]. To ensure the continuity and efficiency of 3D bioprinting, we first tested the printability of alginate-gelatin (AG) bioink after blending with ADSCs and PD ECM solution (Fig. 3A). Representative microscopic images showed that the bioink filaments deposition was precisely controlled and evenly distributed in the 3D constructs even at day 14 (Fig. 3B and Fig. S2C). The structural design of bioprinted constructs was optimized according to previous reports, and ADSCs were well-distributed in the composite matrix, indicating the formation of a specific SG-induced microenvironment similar to our previous report (Fig. 3B, C and Fig. S2D) [32]. Meanwhile, rheological testing also indicated that the addition of ADSCs and PD ECM solution in the bioink conferred shear thinning behavior and gelation time as comparable as the AG hydrogel (Fig. 3D, E and Figs. S2E and F). Furthermore, live-cell imaging revealed more than 85% cell viability in the bioprinted constructs, indicating negligible cell death during extrusion and ionic cross-linking (Figs. S2G and H). At the same time, during the induction culture, the cells can also achieve rapid proliferation and spreading in the 3D matrix (Fig. S2G, I and J).

Then, the capability of 3D-bioprinted specific microenvironments to direct SG differentiation of ADSCs was further investigated. After dissolving bioprinting constructs and isolating cells, expression of the SG markers (containing K8, K14, K18, K19, and ATP1A1) were initially identified with immunofluorescence staining. Representative fluorescent images showed that the SG markers began to appear in 3D constructs at day 1 and continued to day 3, 7 and 14, while most of the SG makers were absent within 14 days in 2D culture systems except for a weak expression of K14 and K18, which suggested the crucial role of 3D administration in SG specification (Fig. 3F, G and Figs. S3A and B). Compared with the culture conditions without specific ECM (2D/ADSC group and 3D/ADSC group), the cells cocultured with PD (2D/ADSC + PD group and 3D/ADSC + PD group) were more likely to form cell clusters (Figs. S3A and B, arrowheads) and had stronger Ca^{2+} transport capacity (Fig. 3G and H).

Moreover, we also confirmed the differentiation status of ADSCs at the transcriptional level. Similar to the immunostaining results, expression of SG marker genes (including *K8*, *K18*, *Atp1a1*, *Aqp5* and *Fxyd2*) in the 3D constructs was higher than the 2D culture condition and increased notably at day 3 and 7 (Fig. 3I and Figs. S3C–E). Over all, iSGCs were obtained by 3D structure and PD synergistical administration. In addition, except for directing SG differentiation, the 3D microenvironment is also conducive to the maturation of the secretory function of iSGCs (Fig. 3F and G). PD could enhance the ion transport function of iSGCs by promoting cell aggregation, as previously confirmed (Fig. 3H and Figs. S3A and B, arrowheads) [32].

3.4. Defining SG-vasculature interplay via noncontact communication

In view of the apparent proangiogenic effects of SGs in CellPhoneDB analysis, we further investigated whether the paracrine signaling from SGs favors vascular network construction or maturation. First, we examined the effect of iSGCs (3D/ADSC + PD group) on the *in vitro* angiogenic activity of DMECs, as well as ADSCs (2D/ADSC group), PD-induced differentiated ADSCs (PD-iADSCs; 2D/ADSC + PD group) and 3D culture induced differentiated ADSCs (3D-iADSCs; 3D/ADSC group) were set as controls. EC chemotaxis is the first process in both vasculogenesis and angiogenesis. Therefore, we first evaluated the effects of

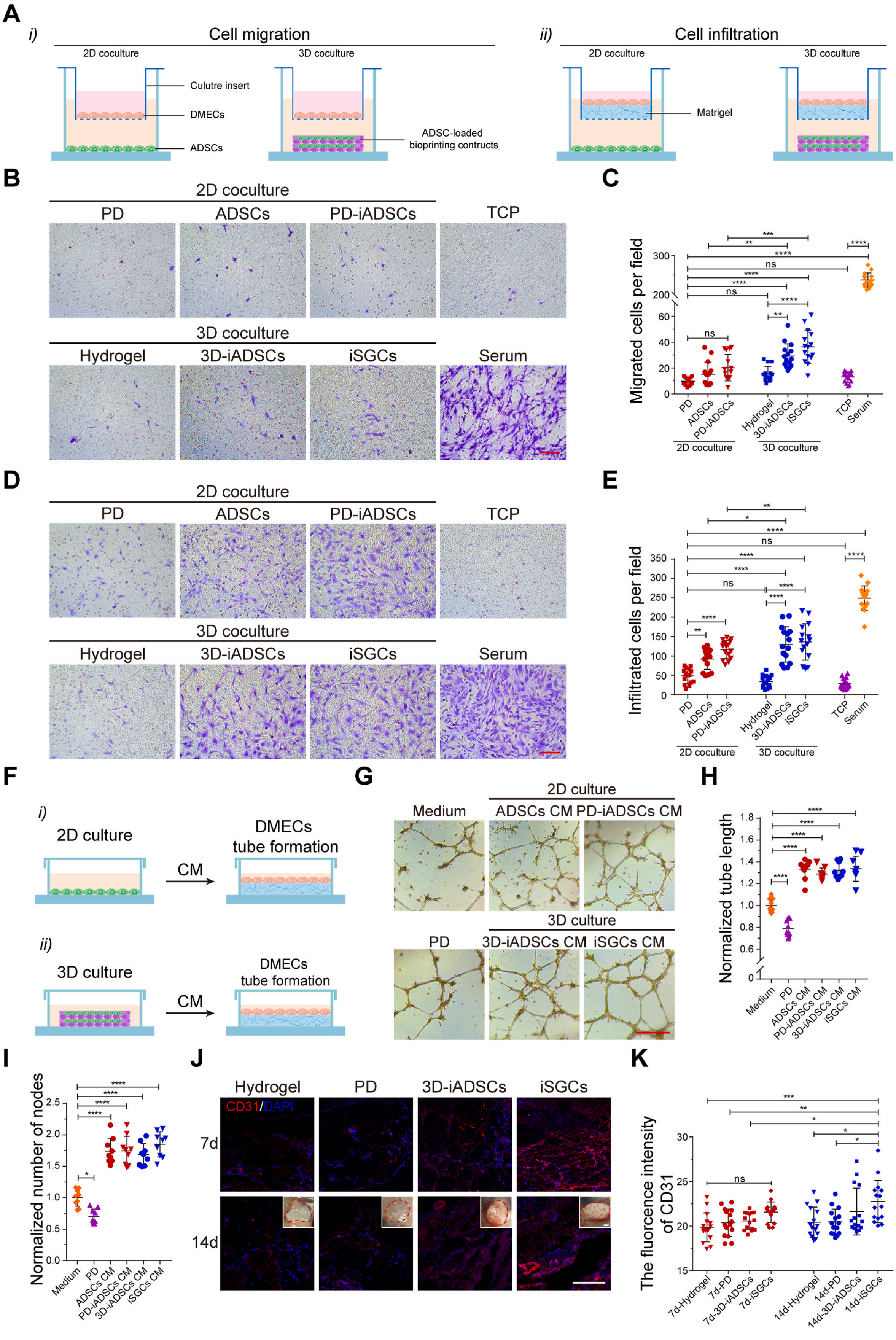

(caption on next page)

Fig. 4. Effects of iSGCs on the angiogenic activity of DMECs. (**A**) Schematic showing the coculture of predifferentiated ADSCs and DMECs and their assessment by Transwell migration and infiltration assays. (**B, C**) Analysis of the chemotactic migration of DMECs in 2D/3D coculture systems after 20 h (n = 15). (**D, E**) Analysis of the chemotactic infiltration of DMECs in 2D/3D coculture systems after 36 h (n = 15). The serum group and TCP group were used as positive and negative controls, respectively. DMECs were stained with crystal violet. (**F**) Schematic showing a tube formation assay with DMECs stimulated by predifferentiated ADSCs. CM, conditioned medium. (**G–I**) Characterization of the capillary-like structures of DMECs cocultured with different CM after 8 h (n = 9). (**J, K**) Investigation of the proangiogenic activity of predifferentiated ADSCs after subcutaneous implantation in mice for 7 and 14 days (n = 15). Insets: photographs of the hydrogel plugs at 14 d after implantation. CD31, red; DAPI, blue. The results are presented as mean ± s.d., $*P < 0.05$, $**P < 0.01$, $***P < 0.001$, $****P < 0.0001$. ns, not significant. The multiple-group comparison was implemented by one- or two-way ANOVA with Tukey's multiple comparisons test. Scale bars: **B**, **D**, 100 μm; **G**, 500 μm; **J**, 200 μm.

iSGCs on EC migration and infiltration *in vitro* (Fig. 4A). DMECs, considered tissue-specific and more responsive to angiogenic factors, were extracted from the skin of newborn mice (Fig. S4), and then exposed to the predifferentiated ADSCs in different coculture systems [43–45]. As observed, the numbers of migrated and infiltrated DMECs in the 3D coculture groups were greater than those in the 2D coculture groups, and iSGCs significantly promoted DMEC migration and infiltration than controls (Fig. 4B–E). Subsequently, we assessed the effect of iSGCs on EC tube formation *in vitro*. As shown in the schematic diagram (Fig. 4F), conditioned media (CM) derived from the cultures under different conditions were used to coculture with the DMECs. Both optical images and quantitative analysis indicated that the capillary-like network in the 3D culture groups, especially in the iSGC group, was denser and more complete than that in the 2D culture groups (Fig. 4G–I). Meanwhile, the expression level of *Vegfa* gene in different differentiated cells also indirectly confirmed these results (Fig. S5).

Next, we investigated the proangiogenic ability of iSGCs *in vivo* using a subcutaneous hydrogel implantation model in mice. We first pretreated the ADSCs with different biochemical (PD) and structural (3D bioprinting structures) cues for 3 days and then subcutaneously implanted them in mice for 7 and 14 days. Compared with the control groups, iSGC-containing hydrogel plugs showed significantly increased $CD31^+$ cells and more mature infiltrated vessels at 7- and 14-days post-implantation, respectively, implying that iSGCs had distinct endothelial chemotaxis, giving rise to microvessels ingrowth (Fig. 4J and K). Taken together, these results reveal that iSGCs have potent proangiogenic ability and indirectly increase the DMEC angiogenic potential via paracrine action [18]. This communication between SGs and the vasculature may regulate the secretion of sets of chemotactic and proangiogenic factors as described above, which stimulate the directional migration of blood vessels and contribute to the anatomical arrangement of SGs and the vasculature.

3.5. Defining SG-vasculature interplay by direct cell-cell interactions

In view of the close spatial location and reciprocal relationship between SGs and their vasculature, we further explored whether direct physical contact could affect the formation and function of SGs and their specific vasculature. We adopted a 3D microfluidic chip to model their physiological environment while simultaneously permitting high-resolution imaging of cell-cell interactional morphogenesis in situ [46–48]. As shown in Fig. 5A, the microfluidic device contained three parallel channels separated by evenly spaced supporting microposts. Matrigel and cells were loaded into the central channel (gel channel, G-C) and side channels, respectively. Matrigel contraction during gelation caused formation of the gel pockets between two posts, which provided a 3D space for cell adhesion and clustering. Upon gelation, ADSCs (t = −3 d) and DMECs (t = 0 d) were sequentially injected into the iSGC-C and DMEC-C, settled into gel pockets, and the mutual migration of iSGCs and DMECs would occur in the following two days (Fig. 5B). In this context, we next designed the strategy in Fig. 5C to clarify the interactions between iSGCs and DMECs. Representative phase-contrast micrographs taken at the scheduled time demonstrated clearly visible directional infiltration and spontaneous aggregation of two types of cells from side channels within Matrigel. Compared with the groups loaded only with ADSCs or DEMCs (DMECs group, 3D-iADSCs group and iSGCs group), sequential addition of the two types of cells promoted rapid mutual chemotaxis and resulted in the formation of well-organized cell clusters (Fig. 5C–E). Besides, K18 immunofluorescent staining also revealed that varying coculture environment induced the formation of remarkably different self-organized morphologies of iSGC clusters (Fig. 5F). Specifically, among all three differentiated ADSCs, iSGCs co-cultured with DMECs achieved the maximum cluster size (Fig. 5F) and the spherical iSGCs clusters were surrounded by DMECs, similar to the spatial and anatomical arrangement of SGs and their adjacent vasculature (Fig. 5C, G).

We further assessed the effect of SG-vasculature interactions on cell function by the expression of specific markers, i.e., ATP1A1 and VE-cadherin (Fig. 5G and H). Although primary ADSCs loaded in the 3D microfluidic chip showed phenotypic adaptation toward the SG lineage, the secretory function of iSGCs was significantly enhanced only upon cocultured with DMECs, as demonstrated by positive ATP1A1 immunostaining. Moreover, compared with the pure DMEC group, the presence of tight junctions between DMECs was also confirmed by positive VE-cadherin immunostaining within the clusters of iSGCs and DMECs. In conclusion, the direct interaction of SG-vasculature not only promotes the construction of glandular structures, but also promotes the maturation of secretory functions.

3.6. Fabrication of dermal ECM scaffolds with angiogenic capability

In recognition, engineering scaffolds with 3D hierarchical pore structure is a significant strategy for host cell infiltration and in situ vascularization [49,50]. To further create a biomimetic model of SG-vasculature *in vitro*, we generated the AES with porous structure for replicating the proximal vascular network of SGs. According to the previous fabrication criteria, intersectional PCL microfibers with diameters of 166.3 ± 19.9 μm were collected for preparing sacrificial templates, as demonstrated by optical images, scanning electron microscopy (SEM) micrographs, fast Fourier transform (FFT) analysis and Nightingale Rose plot (Figs. S6A–C) [40]. Subsequently, the templates were implanted subcutaneously into rats for 4 weeks to guide fibrous tissue ingrowth and ECM deposition. As shown in Fig. 6A, newly formed dermal-like tissue was filled in inter-fiber space, which confirmed by both transverse and longitudinal cross-sections. Following removal of the polymer template and cellular components, AES with porous structure was obtained (Fig. 6A and Fig. S6D). SEM characterization of AES revealed the presence of 3D interconnected network of microchannels, which had an average diameter of 218.6 ± 4.9 μm (Fig. 6A and Fig. S6E). The NES, namely control group, was also prepared by the same method, but the fibers of the sacrificial template were thinner (11.9 ± 1.1 μm) than that of AES (Figs. S6A–D). Compared with the AES, NES possessed a relatively smooth surface and a dense and compact constitution (Fig. 6A, NES). Furthermore, histological staining showed that no nuclei remained inside the AES and NES after decellularization (Fig. 6B, C), and a large amount of collagen, elastin and sulphated glycosaminoglycans were visualized in the ECM scaffolds (Fig. 6D). The quantitative analysis also confirmed that the DNA content in both types of scaffolds were much lower than the minimum standards for acellular products (50 ng mg^{-1}), and most of the ECM components were retained in the scaffolds (Fig. 6E–H) [51].

We next evaluated the angiogenic ability of AES *in vitro* and *in vivo*.

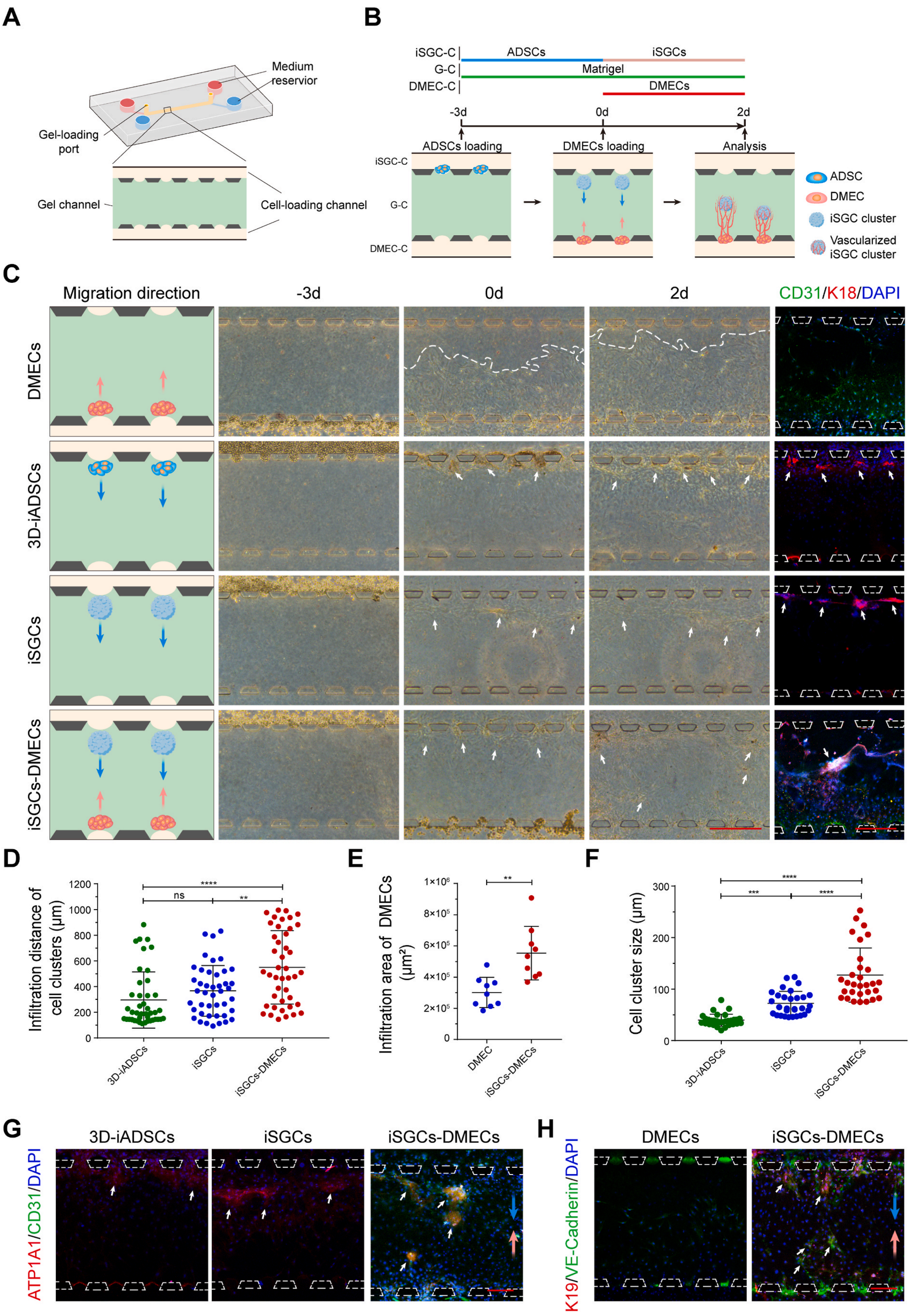

(caption on next page)

Fig. 5. Microfluidic modeling of SG-vasculature interactions. (**A**) Schematic of the 3D microfluidic device. (**B**) Schematic showing the iSGCs-DMECs interactions based on cell chemotaxis in the microfluidic platform. After initial seeding, clustering, and differentiation of ADSCs in iSGC-C ($t = -3$ to 0 d), DMECs were used to supplement the DMEC-C, from $t = 0$ d onward. Representative time-series of zoomed in views of the G-C reveal directional infiltration and spontaneous aggregation of cells from two side channels toward the central channel. (**C**) Schematics of cell configuration and micrographs revealing the iSGCs-DMECs interactions. K18 (red) was applied to label 3D-iADSCs and iSGCs, and CD31 (green) was used to label DMECs. (**D–H**) The mutual benefit of iSGCs and DMECs was explored at $t = 2$ d in terms of infiltration distance (**D**; $n = 43$), infiltration area (**E**; $n = 8$), self-organization (**F**; $n = 30$) and cell function (**G**, **H**). ATP1A1 and K19, red; CD31 and VE-cadherin, green; DAPI, blue. Red and blue arrows indicate the infiltration direction of DMECs and differentiated ADSCs, respectively. White arrows highlight the cell clusters. The dashed line locates the leading tip cells of DMECs within the G-C. Dashed trapezoids emphasize the supporting posts at the Matrigel interface within the side channels. The results are presented as mean ± s.d., $^{**}P < 0.01$, $^{***}P < 0.001$, $^{****}P < 0.0001$. ns, not significant. The two-group comparison was performed by unpaired two-tailed *t*-test. The multiple-group comparison was implemented by one-way ANOVA with Tukey's multiple comparisons test. Scale bars: **C**, 500 μm; **G**, **H**, 200 μm.

For the *in vitro* DMECs infiltration assay, confocal imaging data was imported into Imaris software for extracting the spatial location information of each single cell within scaffolds. When comparing the infiltration depth of DMECs with the NES, the AES group displayed substantially greater average depth of cell infiltration (Fig. 6I and Fig. S6F). For the *in vivo* subcutaneous implantation assay, both AES and NES were subcutaneously implanted into mice for 14 days. Then, all the *in vivo* results, e.g., Laser Doppler blood flow analysis, 3D reconstruction analysis of vascular invasion, hematoxylin-eosin (H&E) staining, and CD31 immunostaining, confirmed the superior ability of AES than NES for facilitating spontaneous in situ vascularization (Fig. 6J and Fig. S6G). Overall, these results demonstrate the excellent angiogenic ability of AES and can provide a tissue-specific vascularization environment for studies of SG-vascular interactions.

3.7. Modeling the vascular niche for reproducible SG regeneration

Based on the sufficient and stable cell source of SGCs and successfully established biomimetic angiogenic platform, we generated a biomimetic SVIM using a stepwise strategy to recapitulate SG-vasculature interactions *in vitro* and broaden their potential for regenerative and translational applications (e.g., SG regeneration, disease modeling, and drug screening) (Fig. 7A). As observed, we first adopted the 3D bioprinting technique with PD ECM to direct SG differentiation of ADSCs. After 3 days of culture, iSGCs were obtained by examining the lineage of induced ADSCs. We then exposed the iSGCs to SGIM to form 3D spheroids using the hanging-drop approach (Fig. 7B–E and Fig. S7). After 3 days of culture in SGIM, the spheroids were gently seeded on the surface of a prevascularized AES for 7 days-culturation, and then used for analysis (Fig. 7F–I).

It is crucial for glandular microvessels to associate with respective secretory coils or ducts in a timely manner to ensure the establishment of sweat transport and absorption apparatus. From this perspective, we investigated whether the iSGC spheroids and DMECs would similarly interact in a dermal-specific microenvironment. As noted, the spheroids were deposited into the pore spaces of AES, and structural integrity was maintained after 7 days of culture, while the spheroids in the NES group stayed on only the surface of the scaffolds (Fig. 7F–H). Meanwhile, a large number of DMECs in the AES migrated toward the iSGC spheroids and wrapped around their surface, which was well aligned with the spatial arrangement of the SG-vasculature anatomy (Figs. 1B and 7I, AES). Conversely, after cocultivation for the same duration, only a few DMECs in the NES group migrated on the surface of the SG spheroids, and most of the cells were located at the boundary of SG spheroids and scaffold (Fig. 7I, NES). This may be due to the fact that iSGC spheres only stay on the surface of NES and lack biochemical and structural guiding cues similar to those inside AES, thus hindering the spontaneous organization process of both. Furthermore, we also examined the tissue-reconstitution capacity and mechanical properties of the SVIM. We transplanted vascularized GFP-labeled iSGC spheroids from the SVIM into the paw pads of mice and found that after 14 days, iSGCs were randomly integrated into the ducts or secretory coils of SGs, which were surrounded by a larger number of capillaries than normal SGs (Figs. 7J and 1C). And the mice treated with iSGC spheroids showed a dramatic increase in the number of dark spots (representing activated sweat pores) on the foot pads within 15 min of the iodine/starch-based sweat test (Fig. 7K). Meanwhile, we also established the SVIM using GFP-labeled ADSCs and Tdtomato-labeled DMECs. The vascularized spheroids were manually collected and transplanted in the thermal-injured mouse model (Fig. S8). During sweat test at day 14, the normal and treatment groups showed black dots on foot pads within 15 min, and no black dots were observed on untreated palm area even after 20 min (Fig. S8A). Similarly, H&E staining also revealed SG-vasculature regeneration in treated group (Fig. S8B). In palmar dermal tissue, Tdtomato-positive microvessels closely surrounded GFP-positive SGs, and their histological structure was similar to normal SGs (Fig. S8C). In addition, the tensile strength of the SVIM was comparable to that of native skin and had the potential for use as an SG-carrying skin substitute (Fig. 7L to N). Collectively, these results validate the robustness of SG-vasculature interactions and emphasize the ability of the vascular niche to promote SG regeneration.

4. Discussion

SGs are the most numerous glands of the human body (200-700 cm^{-2}) and essential for thermoregulation and electrolyte balance [12,14]. Owing to the limited tissue-regenerative capacity, scarcity of donor skin, and low tolerance for *in vitro* amplification and subcultivation, there is no systematic and effective regenerative strategies for SGs in the past few decades [42,52]. Hopefully, increasing studies demonstrate that 3D bioprinting seems to be obvious advantageous for integrating multiple biochemical and biophysical cues spatially for cellular regulation, ensuring complex structures with reproducibility, and stabilizing newly formed tissues [53,54]. 3D architectural support is an indispensable factor in the maintenance of the intercellular interactions, biological characteristics and glandular morphogenesis of SGCs [32,33,55]. Our previous study revealed that SGCs cultured in 3D conditions maintained the biological characteristics of SGCs; however, once deprivation of 3D architectural support, the self-organized formative process was terminated and the cells gradually lost the biological characteristics of SGCs [55]. Thus, the principle of providing 3D spatial support for SGCs was applied to the design of 3D printed block structures and the fabrication of iSGC spheroids. Recently, we developed a 3D bioprinted matrix with PD homogenate to recapitulate the SG regenerative microenvironment, which efficiently direct bone marrow-derived mesenchymal stem cells (BMSCs) differentiation and boost the functional restoration of glandular tissue [32,33]. Despite being a valid approach, this engineered microenvironment still lacks the SG-specific vascular niche, which is crucial for glandular development and sweat transport and absorption [15,20,21]. Furthermore, considering the accessibility and functionality, ADSCs stand as ideal candidates for mesenchymal stem cell-based clinical applications rather than BMSCs [56]. In practice, the medical procedures of lipectomy or simple lipoaspiration are associated with very low donor morbidity and a high available volume of tissue. Regarding functionality, the phenotype of ADSCs is well described and they possess more proangiogenic, anti-apoptotic, antioxidant, and immunomodulatory capacities [57–60]. In this study, we first demonstrated a feasible and reproducible approach

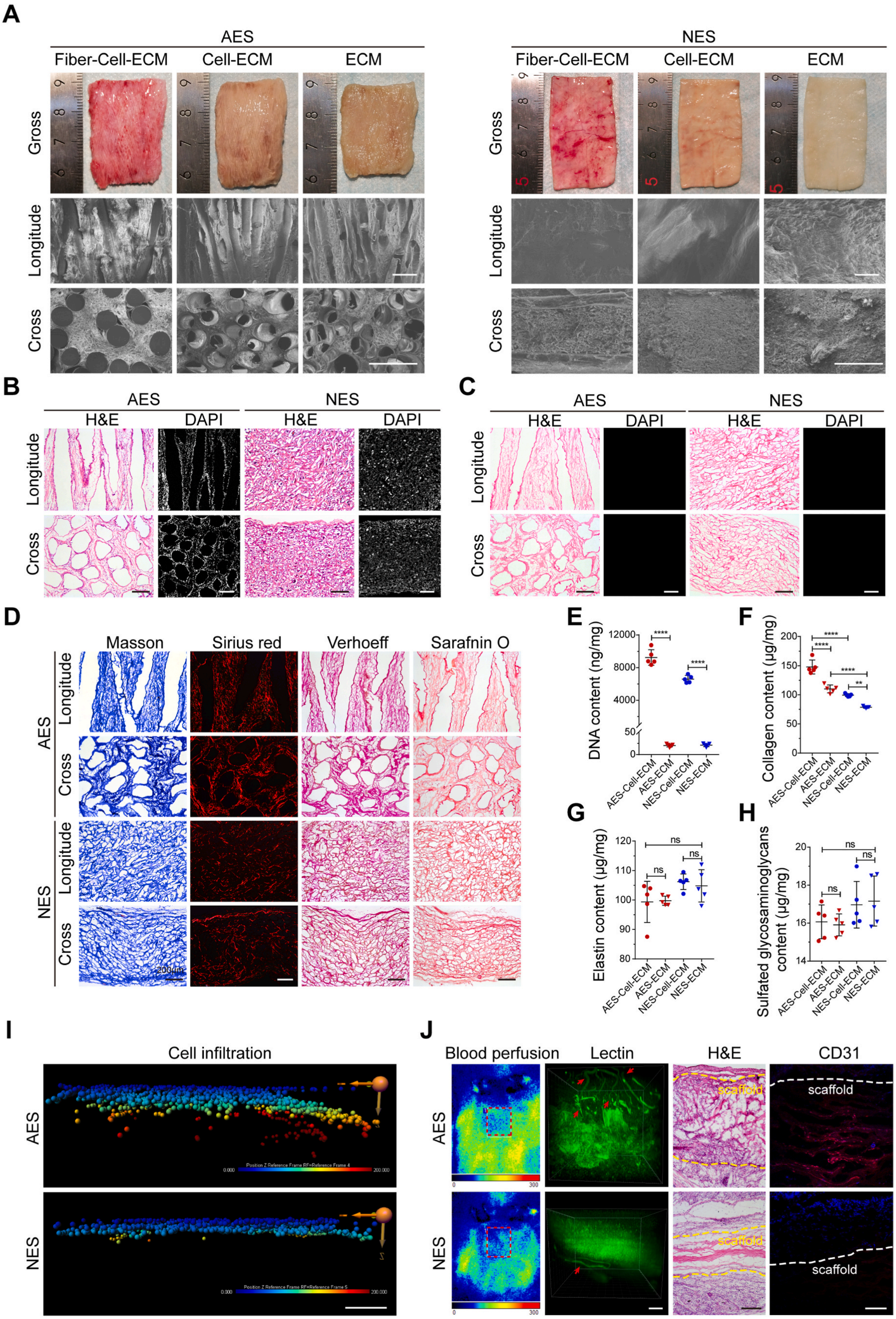

(caption on next page)

Fig. 6. Characterization of the AES and NES. (**A**) The macroscopic morphology (optical images) and microstructure (SEM micrographs) of AES and NES were visualized at different stages of preparation (e.g., Fiber-Cell-ECM, Cell-ECM and ECM). (**B**, **C**) H&E and DAPI staining indicated the nucleus content of AES and NES before and after decellularization. (**D**) Optical imaging identified ECM components of AES and NES stained with Masson trichrome, Sirius red, Verhoeff, and safranin O methods. (**E**–**H**) Dot plots of DNA, collagen, elastin, and glycosaminoglycan revealed nucleic acid and ECM components content before and after AES and NES decellularization (n = 5). (**I**) Representative images of the infiltrated DMECs in AES and NES. 3D reconstruction analysis was performed by replacing each cell with a sphere. Sphere color represents the infiltration depth of cells relative to the monolayer on the scaffold surface. (**J**) Laser Doppler blood flow analysis, 3D reconstruction analysis, H&E staining, and CD31 immunostaining determined the angiogenic ability of AES and NES. The dashed box highlights the subcutaneously implanted scaffolds. The arrows indicate the blood vessels infiltrating into the scaffolds. The dashed lines denote the boundary of scaffolds. Lectin, green; CD31, red; DAPI, blue. Results are presented as mean ± s.d., $^{**}P < 0.01$, $^{****}P < 0.0001$. ns, not significant. The two-group comparison was performed by unpaired two-tailed *t*-test. The multiple-group comparison was implemented by one-way ANOVA with Tukey's multiple comparisons test. Scale bars: **A**, 500 μm; **B-D**, **I**, **J**, 200 μm.

for directing differentiation of ADSCs into iSGCs in a 3D-printed matrix. Then, we achieved the reproducibility of ADSC-differentiated iSGC spheroids and some key features of native skin architecture by 3D bioprinting, integrating the SG-specific vascular network by porous dermal ECM scaffolds. In contrast to conventional tissue engineering approaches of SG regeneration, the present 3D-printing strategy for SG regeneration combination with SG-specific vascular niche offered a more biomimetic microenvironment that promote physiologically relevant glandular morphogenesis *in vitro* and *in vivo*.

Following tissue clearing technique, we firstly mapped the anatomy of SGs and their surrounding microvasculature. Our findings demonstrated that the particularly elaborate capillary networks were tightly arranged around the SGs and these adjacent microvascular networks formed a radial pattern, and follow the contours of SGs tubules closely, which was consistent with the findings of conventional histological studies [13,15,17]. Although SGs display the close proximity with their vascular beds, the significance of this interaction remains elusive. To clarify the interactions between glandular and endothelial cells, we predicted cell-cell communication networks with CellPhoneDB analyzing tool under physiological condition and further recapitulated vascularized features of SG niches *in vitro* to model this interplay. Our findings demonstrated that the reciprocity between vascular and glandular cells is a cornerstone of many physiological processes for maintaining glandular homeostasis and repair capability. The biological functions of the ligand-receptor pairs in SG-vasculature communication mainly involved in chemotaxis, blood vessel development, gland development, wound healing and cell differentiation. Given that, an exploratory pilot study examined the effects of human SG-derived nestin^{+} cells on mortal wound healing in an ex vivo model [19]. It showed that the nestin^{+} SGCs demonstrated the capacity to promote wound healing, including angiogenesis and reepithelialisation significantly. These findings are consistent with the GO analysis results in our study. That is, nestin^{+} SGCs stimulate a variety of resident skin cell populations, including ECs, fibroblasts, and keratinocytes, by releasing various signaling factors that promote proliferation, migration, differentiation, and wound healing, then enable the damaged skin to enter the repair stage such as proliferation and remodeling. Moreover, there are two hypotheses on the mechanisms of SGCs promoting blood vessel development. One was that SG-derived stem cells differentiation into endothelial-like cells directly in proangiogenic environments [18]. The other was that SGCs acted as trophic mediators, thus creating a proangiogenic microenvironment in the resident area (e.g., the release of VEGF) [18,19,61]. CellPhoneDB analysis also uncovered the similar feedback regulation of microvasculature promoting gland development (e.g., the release of TGFB). Bone morphogenetic proteins (BMP) are members of TGFB superfamily present in the mesenchyme and are known to regulate the development of ectodermal appendages [62]. Many findings suggest that inhibiting BMP signaling favors hair follicle cell fates, whereas active BMP signaling promotes glandular cell fates [14]. As an alternative mechanism of contribution, ECs may secrete an amount of TGFB to active the BMP signaling, thus helping to promote SG development. This hypothesis is also in keeping with previously reported that SGs are specified by BMPs and FGFs that signal to epithelial buds and suppress sonic hedgehog production, a hair fate facilitator [63]. Furthermore, other studies also have highlighted the requirement for FGF signaling in the normal development of the prostate gland and lacrimal gland [64,65]. In adult prostate, the maintenance of a functional FGF/FGFR signaling axis is critical for organ homeostasis and function, as its disruption leads to prostate hyperplasia. And both FGF10 and FGF7 were able to initiate budding and branching morphogenesis of lacrimal gland epithelium. Our interplay model exploring the role of the SG vascular niche also revealed physiologically relevant glandular morphogenesis *in vitro* and *in vivo*. Our findings are consistent with the results of previous studies that during development, the growing SGs are accompanied by their specific microvessels extending downward from the subcutaneous vascular plexus and subsequently become surrounded by the cages of newly-formed capillary networks, and these dynamic processes may coordinate through their complicated signaling network and anatomical structure [13].

To further define how SG-vascular interplay is related to regenerative potential, we assessed the effect of SG-vasculature interactions with or without cell-to-cell contact. We found that DMECs surrounded improved SG functional cluster aggregation, and iSGCs also had potent proangiogenic ability and indirectly increased DMEC angiogenic potential via paracrine action. These findings suggest a potentially powerful mechanism for reciprocal regulation between SGs and the vasculature. During development, the vasculature acts as a trophic mediator via not only secreted molecules but also physical contact, thus helping to create a pro-developmental microenvironment for SGs in their residential area. Simultaneously, the growing SGs provide signals for patterning and guidance of blood vessels and subsequently become surrounded by cages of newly formed vascular networks. This interaction may contribute to driving self-organization-related biological events of SGs and their surrounding microvasculature. However, due to the complexity of this interaction, its specific mechanism at the molecular level remains to be elucidated and verified by further *in vitro* and *in vivo* studies.

5. Conclusion

In summary, our findings provide a novel strategy of directing ADSC differentiation for promoting SG regeneration by integrating the SG-specific vascular niche. Our approach to fabricating tissue- or organ-specific vascular niches is a versatile platform for studying their interplay, paving the way for successful functional regeneration. Specifically, our results validate the robustness of SG-vasculature interactions, emphasize the ability of the vasculature to promote SG regeneration and provide a new route for the study of glandular morphogenesis and vasculature reconstruction. Furthermore, innervation is another cue required for the functional integrity of SGs, for eccrine SGs couldn't produce sweat without innervation. Future work may focus on integrating neural factors to construct a more biomimetic model of glandular development *in vitro*, as well as revealing the specific mechanisms by which SGs interact with surrounding structures to promote in situ regeneration of SGs after skin injury.

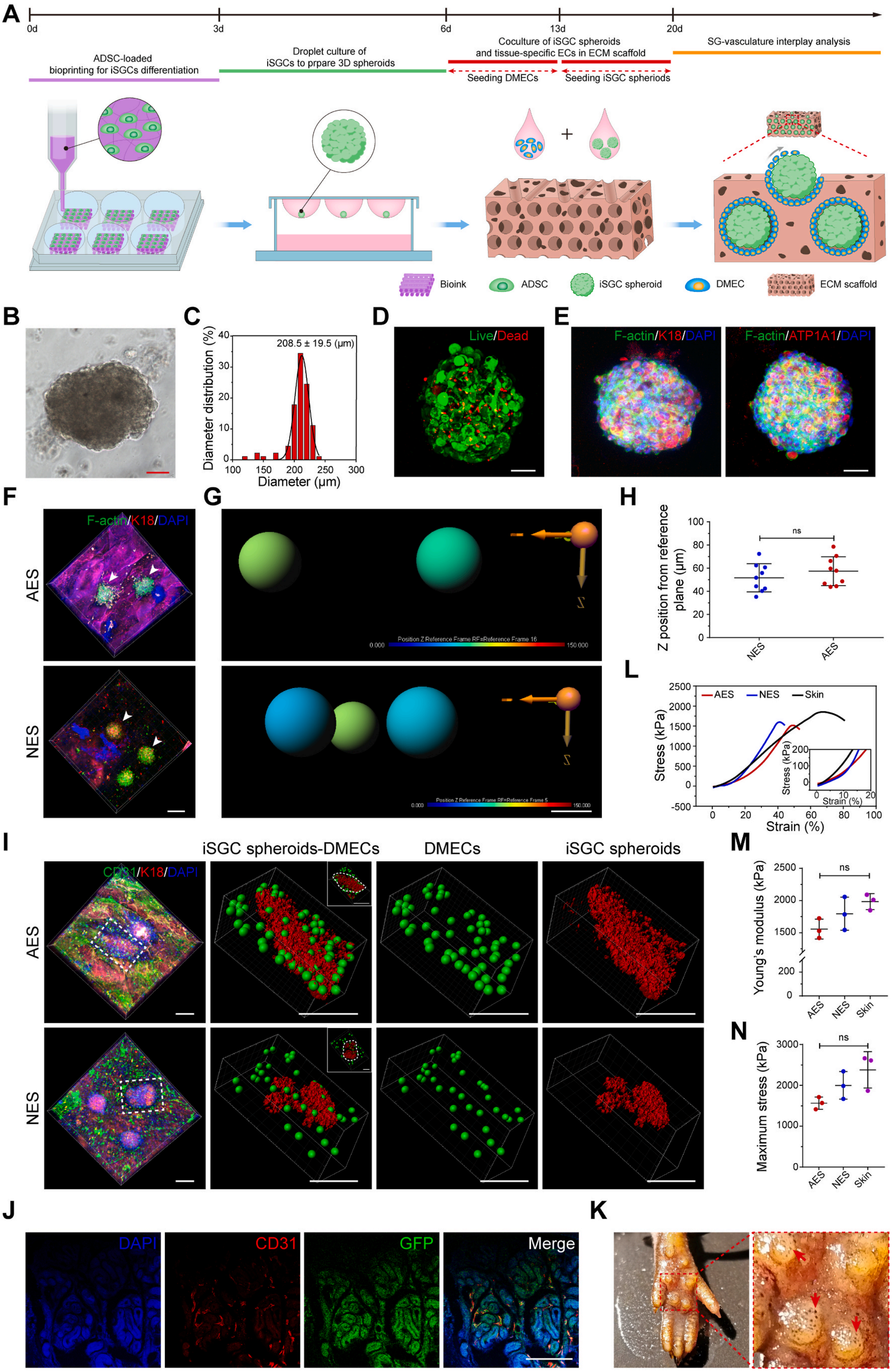

(caption on next page)

Fig. 7. Establishment of a biomimetic SVIM. (**A**) Schematic showing establishment of a biomimetic SVIM *in vitro*. (**B**) Formation of iSGC spheroids using hanging-drop culture. (**C**) The diameter of iSGC spheroids. (**D**, **E**) Identification of the cell viability and lineage of iSGC spheroids. Live cells, F-actin, green; dead cells, K18 and ATP1A1, red; DAPI, blue. (**F**, **G**) Representative fluorescent images and 3D reconstruction diagrams of the infiltrated iSGC spheroids in AES and NES. Arrowheads indicate the iSGC spheroids. 3D image analysis was performed by replacing each iSGC spheroid with a sphere. Sphere color represents the infiltration depth of iSGC spheroids relative to the scaffold surface. F-actin, green; K18, red; DAPI, blue. (**H**) Quantification of the infiltration depth of iSGC spheroids (n = 9). The spatial position information of iSGC spheroids was extracted from the confocal z-stacks using Imaris software. (**I**) 3D reconstruction of the SVIM based on confocal z-stacks. DMECs were replaced with green spheres and iSGC spheroids were replaced with red rough surface. The dashed box highlights the boundary of modeled SVIM. CD31, green; K18, red; DAPI, blue. (**J**) Transplantation of the vascularized GFP-labeled iSGCs spheroids in paw pads of mice to assess their tissue-construction capacity. CD31, red; GFP, green; DAPI, blue. (**K**) Sweat test of mice treated with iSGCs spheroids. Arrows indicate the dark dots on foot pads (representing activated sweat pores). (**L–N**) The mechanical properties of the prevascularized iSGC-bearing scaffolds were further investigated (n = 3). At least three biological replicates of SVIM were carried in this experiment. Results are presented as mean ± s.d. The two-group comparison was performed by unpaired two-tailed *t*-test. The multiple-group comparison was implemented by one-way ANOVA with Tukey's multiple comparisons test. ns, not significant. Scale bars: **B**, **D**, **E**, 50 μm; **F**, 200 μm; **G**, 150 μm; **I**, 200 μm; **J**, 100 μm.

Ethics approval and consent to participat

Human subjects

All normal human skin tissues were obtained from a 5 × 5-mm^2 skin biopsies with the informed consent of the patients, and the studies were approved by the Ethics Committee of the Chinese PLA General Hospital (Beijing, China; project No. ChiCTR2000033157).

Animals

Animals were maintained in a specific-pathogen-free facility of Chinese PLA General Hospital in accordance with the Guide for the Care and Use of Laboratory Animals. All animal experiments were approved by the Institutional Animal Care and Use Committee of Chinese PLA General Hospital (approval number SCXK(BJ)2017–0001).

CRediT authorship contribution statement

Xingyu Yuan: Conceptualization, Methodology, Formal analysis, Investigation, Writing – original draft. **Xianlan Duan:** Methodology, Formal analysis, Investigation, Writing – original draft. **Enhejirigala:** Methodology, Validation, Formal analysis. **Zhao Li:** Methodology, Software, Validation. **Bin Yao:** Conceptualization, Methodology. **Wei Song:** Resources, Investigation. **Yuzhen Wang:** Methodology, Investigation. **Yi Kong:** Software, Data curation. **Shijun Zhu:** Formal analysis, Investigation. **Fanliang Zhang:** Methodology, Investigation. **Liting Liang:** Methodology, Investigation. **Mengde Zhang:** Investigation. **Chao Zhang:** Methodology. **Deling Kong:** Resources. **Meifeng Zhu:** Resources. **Sha Huang:** Conceptualization, Methodology, Supervision, Writing – review & editing, Funding acquisition. **Xiaobing Fu:** Writing – review & editing, Supervision, Funding acquisition.

Declaration of competing interest

None.

Acknowledgments

We thank D. Kong and M. Zhu for providing the spinning apparatus; D. Zhang for help with tissue clearing measurement; J. Zhang for help with DMEC isolation; J. Li for help with SG induction; and L. Li for help with microfluidic chip preparation. This study was supported by grants from the National Natural Science Foundation of China (81830064, 81721092, 32000969, 82002056), Key Support Program for Growth Factor Research (SZYZ-TR-03), Chinese PLA General Hospital for Military Medical Innovation Research Project (CX-19026), the CAMS Innovation Fund for Medical Sciences (CIFMS, 2019-I2M-5-059), the Military Medical Research and Development Projects (AWS17J005), and Beijing Natural Science Foundation (7204306).

Abbreviations

SG	sweat gland
SGCs	sweat gland cells
3D	three-dimensional
ADSCs	adipose-derived mesenchymal stem cells
DMECs	dermal microvascular endothelial cells
PCL	poly(ε-caprolactone)
ECM	extracellular matrix
PBS	phosphate buffered saline
GO	Gene Ontology
PD	plantar dermis
DMEM	Dulbecco's modified Eagle medium
SGIM	SG induction medium
AES	angiogenic ECM scaffolds
NES	nonangiogenic ECM scaffolds
SVIM	SG-vasculature interaction model
iSGC	induced sweat gland cell
EGM-2	endothelial cell growth medium-2
K	keratin
GFP	green fluorescent protein
TCP	tissue culture plate
iSGC-C	iSGC-loaded channel
DMEC-C	DMEC-loaded channel
VE-cadherin	vascular endothelial cadherin
DAPI	4′,6-diamidino-2-phenylindole
s.d.	standard deviation
ANOVA	analysis of variance
ECs	endothelial cells
VEGF	vascular endothelial growth factor
VEGFR	vascular endothelial growth factor receptor
TGFB	transforming growth factor beta
TGFBR	transforming growth factor beta receptor
IGF	insulin like growth factor
IGFR	insulin like growth factor receptor
FGF	fibroblast growth factor
FGFR	fibroblast growth factor receptor
AG	alginate-gelatin
CM	conditioned media
G-C	gel channel
SEM	scanning electron microscopy
FFT	fast Fourier transform
H&E	hematoxylin-eosin
BMSCs	bone marrow-derived mesenchymal stem cells

Appendix A. Supplementary data

Supplementary data to this article can be found online at https://doi.org/10.1016/j.bioactmat.2022.08.021.

References

[1] S. Rafii, J.M. Butler, B.S. Ding, Angiocrine functions of organ-specific endothelial cells, Nature 529 (7586) (2016) 316–325, https://doi.org/10.1038/nature17040.

[2] X. Sun, W. Altalhi, S.S. Nunes, Vascularization strategies of engineered tissues and their application in cardiac regeneration, Adv. Drug Deliv. Rev. 96 (2016) 183–194, https://doi.org/10.1016/j.addr.2015.06.001.

[3] D.S.Y. Lin, F. Guo, B. Zhang, Modeling organ-specific vasculature with organ-on-a-chip devices, Nanotechnology 30 (2) (2019), 024002, https://doi.org/10.1088/1361-6528/aae7de.

[4] J. Fu, D.A. Wang, In situ organ-specific vascularization in tissue engineering, Trends Biotechnol. 36 (8) (2018) 834–849, https://doi.org/10.1016/j.tibtech.2018.02.012.

[5] H.G. Augustin, G.Y. Koh, Organotypic vasculature: from descriptive heterogeneity to functional pathophysiology, Science 357 (6353) (2017), https://doi.org/10.1126/science.aal2379.

[6] J. Nguyen, Y.Y. Lin, S. Gerecht, The next generation of endothelial differentiation: tissue-specific ECs, Cell Stem Cell 28 (7) (2021) 1188–1204, https://doi.org/10.1016/j.stem.2021.05.002.

[7] J. Kalucka, L. de Rooij, J. Goveia, K. Rohlenova, S.J. Dumas, E. Meta, et al., Single-cell transcriptome atlas of murine endothelial cells, Cell 180 (4) (2020) 764–779, https://doi.org/10.1016/j.cell.2020.01.015, e20.

[8] T. Tajima, S. Morikawa, A. Nakamura, Clinical features and molecular basis of pseudohypoaldosteronism type 1, Clin. Pediatr. Endocrinol. : case reports and clinical investigations : official journal of the Japanese Society for Pediatric Endocrinology 26 (3) (2017) 109–117, https://doi.org/10.1297/cpe.26.109.

[9] R.S. Lacruz, S. Feske, Diseases caused by mutations in ORAI1 and STIM1, Ann. N. Y. Acad. Sci. 1356 (2015) 45–79, https://doi.org/10.1111/nyas.12938.

[10] F.R. Romero, G.R. Haddad, H.A. Miot, D.C. Cataneo, Palmar hyperhidrosis: clinical, pathophysiological, diagnostic and therapeutic aspects, An. Bras. Dermatol. 91 (6) (2016) 716–725, https://doi.org/10.1590/abd1806-4841.20165358.

[11] C. Zhang, Y. Chen, X. Fu, Sweat gland regeneration after burn injury: is stem cell therapy a new hope? Cytotherapy 17 (5) (2015) 526–535, https://doi.org/10.1016/j.jcyt.2014.10.016.

[12] C.P. Lu, L. Polak, A.S. Rocha, H.A. Pasolli, S.C. Chen, N. Sharma, et al., Identification of stem cell populations in sweat glands and ducts reveals roles in homeostasis and wound repair, Cell 150 (1) (2012) 136–150, https://doi.org/10.1016/j.cell.2012.04.045.

[13] O. Yamamoto, Three-dimensional architecture of the microvasculature in the rat foot-pad, with special reference to vasculature around the eccrine sweat glands. A scanning electron-microscopic study of corrosion casts, Cell Tissue Res. 262 (2) (1990) 225–232, https://doi.org/10.1007/bf00309877.

[14] C. Lu, E. Fuchs, Sweat gland progenitors in development, homeostasis, and wound repair, Cold Spring Harb Perspect Med 4 (2) (2014), https://doi.org/10.1101/cshperspect.a015222.

[15] R.A. Ellis, W. Montagna, H. Fanger, Histology and cytochemistry of human skin. XIV. The blood supply of the cutaneous glands, J. Invest. Dermatol. 30 (3) (1958) 137–145, https://doi.org/10.1038/jid.1958.26.

[16] D.C. Quick, W.R. Kennedy, K.S. Yoon, Ultrastructure of the secretory epithelium, nerve fibers, and capillaries in the mouse sweat gland, Anat. Rec. 208 (4) (1984) 491–499, https://doi.org/10.1002/ar.1092080404.

[17] W.R. Kennedy, G. Wendelschafer-Crabb, T.C. Brelje, Innervation and vasculature of human sweat glands: an immunohistochemistry-laser scanning confocal fluorescence microscopy study, J. Neurosci. : the official journal of the Society for Neuroscience 14 (11 Pt 2) (1994) 6825–6833, https://doi.org/10.1523/jneurosci.14-11-06825.1994.

[18] S. Danner, M. Kremer, A.E. Petschnik, S. Nagel, Z. Zhang, U. Hopfner, et al., The use of human sweat gland-derived stem cells for enhancing vascularization during dermal regeneration, J. Invest. Dermatol. 132 (6) (2012) 1707–1716, https://doi.org/10.1038/jid.2012.31.

[19] T. Liao, J. Lehmann, S. Sternstein, A. Yay, G. Zhang, A.E. Matthiessen, et al., Nestin (+) progenitor cells isolated from adult human sweat gland stroma promote reepithelialisation and may stimulate angiogenesis in wounded human skin ex vivo, Arch. Dermatol. Res. 311 (4) (2019) 325–330, https://doi.org/10.1007/s00403-019-01889-x.

[20] A.F. Palazzo, R. Kurata, S. Futaki, I. Nakano, F. Fujita, A. Tanemura, et al., Three-dimensional cell shapes and arrangements in human sweat glands as revealed by whole-mount immunostaining, PLoS One 12 (6) (2017), https://doi.org/10.1371/journal.pone.0178709.

[21] M. Zhang, H. Li, L. Chen, S. Fang, S. Xie, C. Lin, Three-dimensional reconstructed eccrine sweat glands with vascularization and cholinergic and adrenergic innervation, J. Mol. Histol. 49 (4) (2018) 339–345, https://doi.org/10.1007/s10735-018-9773-4.

[22] R. Cai, C. Pan, A. Ghasemigharagoz, M.I. Todorov, B. Forstera, S. Zhao, et al., Panoptic imaging of transparent mice reveals whole-body neuronal projections and skull-meninges connections, Nat. Neurosci. 22 (2) (2019) 317–327, https://doi.org/10.1038/s41593-018-0301-3.

[23] L. Shi, M. Wei, Y. Miao, N. Qian, L. Shi, R.A. Singer, et al., Highly-multiplexed volumetric mapping with Raman dye imaging and tissue clearing, Nat. Biotechnol. (2021), https://doi.org/10.1038/s41587-021-01041-z.

[24] D. Jing, S. Zhang, W. Luo, X. Gao, Y. Men, C. Ma, et al., Tissue clearing of both hard and soft tissue organs with the PEGASOS method, Cell Res. 28 (8) (2018) 803–818, https://doi.org/10.1038/s41422-018-0049-z.

[25] M. Efremova, M. Vento-Tormo, S.A. Teichmann, R. Vento-Tormo, CellPhoneDB: inferring cell-cell communication from combined expression of multi-subunit ligand-receptor complexes, Nat. Protoc. 15 (4) (2020) 1484–1506, https://doi.org/10.1038/s41596-020-0292-x.

[26] S. Davidson, M. Efremova, A. Riedel, B. Mahata, J. Pramanik, J. Huuhtanen, et al., Single-cell RNA sequencing reveals a dynamic stromal niche that supports tumor growth, Cell Rep. 31 (7) (2020), https://doi.org/10.1016/j.celrep.2020.107628.

[27] R. Vento-Tormo, M. Efremova, R.A. Botting, M.Y. Turco, M. Vento-Tormo, K. B. Meyer, et al., Single-cell reconstruction of the early maternal-fetal interface in humans, Nature 563 (7731) (2018) 347–353, https://doi.org/10.1038/s41586-018-0698-6.

[28] J. Rouwkema, A. Khademhosseini, Vascularization and angiogenesis in tissue engineering: beyond creating static networks, Trends Biotechnol. 34 (9) (2016) 733–745, https://doi.org/10.1016/j.tibtech.2016.03.002.

[29] E.C. Novosel, C. Kleinhans, P.J. Kluger, Vascularization is the key challenge in tissue engineering, Adv. Drug Deliv. Rev. 63 (4–5) (2011) 300–311, https://doi.org/10.1016/j.addr.2011.03.004.

[30] A. Dellaquila, C. Le Bao, D. Letourneur, T. Simon-Yarza, In vitro strategies to vascularize 3D physiologically relevant models, Adv. Sci. 8 (19) (2021), e2100798, https://doi.org/10.1002/advs.202100798.

[31] S. Vijayavenkataraman, W.C. Yan, W.F. Lu, C.H. Wang, J.Y.H. Fuh, 3D bioprinting of tissues and organs for regenerative medicine, Adv. Drug Deliv. Rev. 132 (2018) 296–332, https://doi.org/10.1016/j.addr.2018.07.004.

[32] B. Yao, R. Wang, Y. Wang, Y. Zhang, T. Hu, W. Song, et al., Biochemical and structural cues of 3D-printed matrix synergistically direct MSC differentiation for functional sweat gland regeneration, Sci. Adv. 6 (10) (2020), eaaz1094, https://doi.org/10.1126/sciadv.aaz1094.

[33] Y. Zhang, Enhejirigala, B. Yao, Z. Li, W. Song, J. Li, et al., Using bioprinting and spheroid culture to create a skin model with sweat glands and hair follicles, Burns Trauma 9 (2021), https://doi.org/10.1093/burnst/tkab013 tkab013.

[34] S. Huang, B. Yao, J. Xie, X. Fu, 3D bioprinted extracellular matrix mimics facilitate directed differentiation of epithelial progenitors for sweat gland regeneration, Acta Biomater. 32 (2016) 170–177, https://doi.org/10.1016/j.actbio.2015.12.039.

[35] M.M. De Santis, H.N. Alsafadi, S. Tas, D.A. Bolukbas, S. Prithiviraj, I.A.N. Da Silva, et al., Extracellular-matrix-reinforced bioinks for 3D bioprinting human tissue, Adv. Mater. (2020), e2005476, https://doi.org/10.1002/adma.202005476.

[36] N. van Gastel, S. Stegen, G. Eelen, S. Schoors, A. Carlier, V.W. Daniels, et al., Lipid availability determines fate of skeletal progenitor cells via SOX9, Nature 579 (7797) (2020) 111–117, https://doi.org/10.1038/s41586-020-2050-1.

[37] A. Centonze, S. Lin, E. Tika, A. Sifrim, M. Fioramonti, M. Malfait, et al., Heterotypic cell-cell communication regulates glandular stem cell multipotency, Nature 584 (7822) (2020) 608–613, https://doi.org/10.1038/s41586-020-2632-y.

[38] B. Yao, T. Hu, X. Cui, W. Song, X. Fu, S. Huang, Enzymatically degradable alginate/gelatin bioink promotes cellular behavior and degradation in vitro and in vivo, Biofabrication 11 (4) (2019), 045020, https://doi.org/10.1088/1758-5090/ab38ef.

[39] Y. Liu, J. Li, B. Yao, Y. Wang, R. Wang, S. Yang, et al., The stiffness of hydrogel-based bioink impacts mesenchymal stem cells differentiation toward sweat glands in 3D-bioprinted matrix, Mater Sci Eng C Mater Biol Appl 118 (2021), 111387, https://doi.org/10.1016/j.msec.2020.111387.

[40] M. Zhu, W. Li, X. Dong, X. Yuan, A.C. Midgley, H. Chang, et al., In vivo engineered extracellular matrix scaffolds with instructive niches for oriented tissue regeneration, Nat. Commun. 10 (1) (2019) 4620, https://doi.org/10.1038/s41467-019-12545-3.

[41] K.B. Celie, Y. Toyoda, X. Dong, K.A. Morrison, P. Zhang, O. Asanbe, et al., Microstructured hydrogel scaffolds containing differential density interfaces promote rapid cellular invasion and vascularization, Acta Biomater. 91 (2019) 144–158, https://doi.org/10.1016/j.actbio.2019.04.027.

[42] J. Diao, J. Liu, S. Wang, M. Chang, X. Wang, B. Guo, et al., Sweat gland organoids contribute to cutaneous wound healing and sweat gland regeneration, Cell Death Dis. 10 (3) (2019) 238, https://doi.org/10.1038/s41419-019-1485-5.

[43] J. Bourland, D. Mayrand, N. Tremblay, V.J. Moulin, J. Fradette, F.A. Auger, Isolation and culture of human dermal microvascular endothelial cells, Methods Mol. Biol. 1993 (2019) 79–90, https://doi.org/10.1007/978-1-4939-9473-1_7.

[44] H. Hou, J. Li, L. Zhou, J. Liang, J. Wang, J. Li, et al., An effective method of isolating microvascular endothelial cells from the human dermis, Cell Biol. Int. (2020), https://doi.org/10.1002/cbin.11448.

[45] A.R. Calabria, C. Weidenfeller, A.R. Jones, H.E. de Vries, E.V. Shusta, Puromycin-purified rat brain microvascular endothelial cell cultures exhibit improved barrier properties in response to glucocorticoid induction, J. Neurochem. 97 (4) (2006) 922–933, https://doi.org/10.1111/j.1471-4159.2006.03793.x.

[46] Y. Zheng, X. Xue, Y. Shao, S. Wang, S.N. Esfahani, Z. Li, et al., Controlled modelling of human epiblast and amnion development using stem cells, Nature 573 (7774) (2019) 421–425, https://doi.org/10.1038/s41586-019-1535-2.

[47] Y. Zheng, Y. Sun, X. Yu, Y. Shao, P. Zhang, G. Dai, et al., Angiogenesis in liquid tumors: an in vitro assay for leukemic-cell-induced bone marrow angiogenesis, Adv Healthc Mater 5 (9) (2016) 1014–1024, https://doi.org/10.1002/adhm.201501007.

[48] Y. Zheng, Y. Shao, J. Fu, A microfluidics-based stem cell model of early post-implantation human development, Nat. Protoc. 16 (1) (2021) 309–326, https://doi.org/10.1038/s41596-020-00417-w.

[49] A. Mostafavi, M. Samandari, M. Karvar, M. Ghovvati, Y. Endo, I. Sinha, et al., Colloidal multiscale porous adhesive (bio)inks facilitate scaffold integration, Appl. Phys. Rev. 8 (4) (2021), https://doi.org/10.1063/5.0062823.

[50] H. Joukhdar, A. Seifert, T. Jungst, J. Groll, M.S. Lord, J. Rnjak-Kovacina, Ice templating soft matter: fundamental principles and fabrication approaches to tailor pore structure and morphology and their biomedical applications, Adv. Mater. 33 (34) (2021), e2100091, https://doi.org/10.1002/adma.202100091.

[51] P.M. Crapo, T.W. Gilbert, S.F. Badylak, An overview of tissue and whole organ decellularization processes, Biomaterials 32 (12) (2011) 3233–3243, https://doi.org/10.1016/j.biomaterials.2011.01.057.

[52] Q. Sun, X.M. Deng, Y.L. Wang, Y.F. Zhen, F. Li, R.H. Chen, et al., Serum is an indispensable factor in the maintenance of the biological characteristics of sweat gland cells, Mol. Med. Rep. 16 (3) (2017) 2691–2699, https://doi.org/10.3892/mmr.2017.6909.

[53] C.H. Lee, S.A. Rodeo, L.A. Fortier, C. Lu, C. Erisken, J.J. Mao, Protein-releasing polymeric scaffolds induce fibrochondrocytic differentiation of endogenous cells for knee meniscus regeneration in sheep, Sci. Transl. Med. 6 (266) (2014) 266ra171, https://doi.org/10.1126/scitranslmed.3009696.

[54] H. Donnelly, M. Salmeron-Sanchez, M.J. Dalby, Designing stem cell niches for differentiation and self-renewal, J. R. Soc. Interface 15 (145) (2018), https://doi.org/10.1098/rsif.2018.0388.

[55] N. Liu, S. Huang, B. Yao, J. Xie, X. Wu, X. Fu, 3D bioprinting matrices with controlled pore structure and release function guide in vitro self-organization of sweat gland, Sci. Rep. 6 (2016), 34410, https://doi.org/10.1038/srep34410.

[56] A.T. Maria, M. Maumus, A. Le Quellec, C. Jorgensen, D. Noel, P. Guilpain, Adipose-derived mesenchymal stem cells in autoimmune disorders: state of the art and perspectives for systemic sclerosis, Clin. Rev. Allergy Immunol. 52 (2) (2017) 234–259, https://doi.org/10.1007/s12016-016-8552-9.

[57] M. Strioga, S. Viswanathan, A. Darinskas, O. Slaby, J. Michalek, Same or not the same? Comparison of adipose tissue-derived versus bone marrow-derived mesenchymal stem and stromal cells, Stem Cell. Dev. 21 (14) (2012) 2724–2752, https://doi.org/10.1089/scd.2011.0722.

[58] W.S. Kim, B.S. Park, J.H. Sung, The wound-healing and antioxidant effects of adipose-derived stem cells, Expet Opin. Biol. Ther. 9 (7) (2009) 879–887, https://doi.org/10.1517/14712590903039684.

[59] W.S. Kim, B.S. Park, H.K. Kim, J.S. Park, K.J. Kim, J.S. Choi, et al., Evidence supporting antioxidant action of adipose-derived stem cells: protection of human dermal fibroblasts from oxidative stress, J. Dermatol. Sci. 49 (2) (2008) 133–142, https://doi.org/10.1016/j.jdermsci.2007.08.004.

[60] J. Rehman, D. Traktuev, J. Li, S. Merfeld-Clauss, C.J. Temm-Grove, J.E. Bovenkerk, et al., Secretion of angiogenic and antiapoptotic factors by human adipose stromal cells, Circulation 109 (10) (2004) 1292–1298, https://doi.org/10.1161/01.Cir.0000121425.42966.F1.

[61] J.H. Distler, A. Hirth, M. Kurowska-Stolarska, R.E. Gay, S. Gay, O. Distler, Angiogenic and angiostatic factors in the molecular control of angiogenesis, Q. J. Nucl. Med. : official publication of the Italian Association of Nuclear Medicine (AIMN) [and] the International Association of Radiopharmacology (IAR) 47 (3) (2003) 149–161.

[62] V.A. Botchkarev, A.A. Sharov, BMP signaling in the control of skin development and hair follicle growth, Differentiation; research in biological diversity 72 (9–10) (2004) 512–526, https://doi.org/10.1111/j.1432-0436.2004.07209005.x.

[63] C.P. Lu, L. Polak, B.E. Keyes, E. Fuchs, Spatiotemporal antagonism in mesenchymal-epithelial signaling in sweat versus hair fate decision, Science 354 (6319) (2016), https://doi.org/10.1126/science.aah6102.

[64] A. Giacomini, E. Grillo, S. Rezzola, D. Ribatti, M. Rusnati, R. Ronca, et al., The FGF/FGFR system in the physiopathology of the prostate gland, Physiol. Rev. 101 (2) (2021) 569–610, https://doi.org/10.1152/physrev.00005.2020.

[65] A. Garg, X. Zhang, Lacrimal gland development: from signaling interactions to regenerative medicine, Dev. Dynam. : an official publication of the American Association of Anatomists 246 (12) (2017) 970–980, https://doi.org/10.1002/dvdy.24551.